

**AD-A243 166**



**DTIC**

**ELECTE**

**DEC 10 1991**

**S**

**C**

**D**

(1)

**October 1991**

**MTR11230**

**C. Phillip McClay  
Steven Soares  
Peter S. Weitzman**

**Superconducting  
Microwave  
Transmission Lines**

Approved for public release;  
distribution unlimited.

**MITRE**

**The MITRE Corporation  
Bedford, Massachusetts**

**91-17487**



**91 1209 127**

October 1991

MTR11230

C. Phillip McClay  
Steven Soares  
Peter S. Weitzman

Superconducting  
Microwave  
Transmission Lines

CONTRACT SPONSOR MITRE Sponsored Research  
CONTRACT NO. N/A  
PROJECT NO. 91080  
DEPT. D094

Approved for public release;  
distribution unlimited.

**MITRE**

The MITRE Corporation  
Bedford, Massachusetts

Accession For	
NTIS GRA&I	<input checked="" type="checkbox"/>
DTIC TAB	<input type="checkbox"/>
Unannounced	<input type="checkbox"/>
Justification	
By	
Distribution/	
Availability Codes	
Dist	Avail and/or Special
A-1	



Department Approval: Harold S. Bullock

MITRE Project Approval: Joel M. Brown

## ABSTRACT

Superconducting microwave transmission lines can be designed to have lower loss, lower dispersion, and lower phase velocity than conventional metal lines. These properties make superconducting transmission lines attractive for use in many devices and systems such as filters and analog to digital converters. The problem with designing microwave circuits which utilize these lines is that accurate circuit models do not exist. This paper presents models for the microwave transmission line parameters (phase velocity, attenuation, and characteristic impedance) of superconducting lines as a function of temperature and geometry. An experiment to verify these models is also presented.

## **ACKNOWLEDGMENTS**

We would like to thank Bud Babbitt, Ron Haberkorn, Al Montgomery and Joel Schoen for reviewing this report and supporting the work. We would also like to thank Jeff Jones for fabricating the normal conductor MIC resonator. Finally, we would like to thank Jim Rautio of Sonnet Software for providing valuable insight into his electromagnetic simulation program, as well as modifying his program to accept complex surface impedance at our suggestion.

## TABLE OF CONTENTS

SECTION	PAGE
1 Introduction	1
2 Superconducting Transmission Lines	3
2.1 Superconducting Surface Impedance	3
2.2 Transmission Line Models	10
2.3 Transmission Line Characterization Techniques	15
3 Proposed Experiments	21
3.1 Normal Conductor Resonator Measurements	21
3.2 Superconducting Transmission Line Geometry	23
3.3 Dielectric Step Coupled Resonator	26
3.3.1 Resonator Design	26
3.3.2 Impedance Matching Network	29
3.3.3 Substrate Resonances	42
3.3.4 Summary	47
4 Conclusion/Recommendations	51
List of References	53
Glossary	57
Distribution List	59

## LIST OF FIGURES

FIGURE	PAGE
1 Microstrip Geometry	2
2 Coplanar Waveguide Geometry	2
3 Superconducting Impedance Equivalent Circuit	5
4 Relative Complex Conductivity Versus Frequency	8
5 Superconducting Surface Impedance Versus Frequency	9
6 Superconducting and Normal Skin Depth Versus Frequency	9
7 Attenuation as a Function of Frequency for a Microstrip Transmission Line	13
8 Microstrip Phase Constant Versus Dielectric Thickness	13
9 Microstrip Characteristic Impedance Versus Dielectric Thickness	14
10 Reflection Coefficient of a Resonator Plotted on the Smith Chart	19
11 Microstrip Resonator Test Circuit	22
12 Gap Coupling in Thin Dielectric Microstrip	24
13 Impedance Mismatch Coupled Resonator	25
14 Geometry of a Dielectric Step Coupled Microstrip Resonator	27
15 Frequency Response of Dielectric Step Coupled Resonators	28
16 Modified Coplanar Waveguide	30
17 Microstrip with Gap in Ground Plane	30
18 Plots of Impedance Versus Position for the Four-Taper Profiles	32
19 Responses of Four Transformers Using 0.5 Phase Velocity	34
20 Reflection Coefficient of Four Transformers Using 0.5 Phase Velocity	35

<b>FIGURE</b>	<b>PAGE</b>
21 Transformer Response Using Exact Calculation of Phase Velocity	41
22 Transformer Responses Using Exact Calculation of Phase Velocity	42
23 Plot of Top Plate and Gap for the Sinusoidal Transformer	43
24 Substrate and Ports Used by McGinnis and Beyer	44
25 Isolated Ports on a 25-mm by 25-mm Dielectric Slab	45
26 Isolated Ports on a 30-mm by 0.5-mm Dielectric Slab	46
27 Complete Dielectric Step Coupled Resonator	47
28 Complete Dielectric Step Coupled Resonator, Top and Cross-Sectional Views	49



## LIST OF TABLES

TABLE	PAGE
1 Simulated and Measured Data for the Duroid Resonators	22
2 Inputs to Taper Routine	40
3 Summary of Output from Taper Routine	41

## SECTION 1

### INTRODUCTION

The work described in this report was performed as part of project 91080, "Superconducting Analog-to-Digital Converters." One class of superconducting analog-to-digital converters (SADCs) utilize Josephson junctions, transmission lines, and filters consisting of metal in a superconducting state. In order to design SADCs, good models for superconducting microwave transmission lines must exist. This work focuses on modeling superconducting planar microwave transmission lines and designing experiments to verify these models.

Microwave transmission lines fabricated with superconducting material have several advantages over conventional transmission lines. Superconductors exhibit zero resistance at DC and the resistance increases with the square of the frequency. At microwave frequencies, the surface resistance of superconducting niobium is still three orders of magnitude smaller than that of copper at 4.2 K [1]. Thus, smaller microwave filters with higher Q-factors for monolithic microwave integrated circuit (MMIC) applications can be realized by using superconducting material. In addition to low loss, superconducting metals exhibit kinetic inductance associated with the magnetic fields stored in the superconductor. This kinetic inductance can be utilized to fabricate transmission lines with phase velocities as small as 1/100th of the speed of light [2].

Planar transmission lines compatible with SADC designs include Microstrip (MS), Coplanar Waveguide (CPW), Coplanar Strips (CPS), and slotline. The superconducting transmission line models we have developed are general and apply to any geometry of transmission line. Kinetic inductance effects are easiest to measure in MS geometry. For this reason the experimental portion of this study has focused primarily on MS. Kinetic inductance MS lines have extremely low characteristic impedances and for this reason we have analyzed CPW as a high-impedance to low-impedance transition from our 50-ohm measurement system to MS. The geometry of MS and CPW lines are illustrated in figures 1 and 2.

There are no commercially available computer aided design (CAD) tools for microwave design that accurately model the unique properties of superconductors. We have developed a capability for modeling elementary superconducting transmission lines, including the accurate simulation of complex conductivity as a function of temperature and frequency. In section 2 of this paper, these models are presented. These models produce results which can be incorporated into microwave circuit design programs such as Touchstone or Supercompact. Experiments must be performed to confirm the validity of our models. A general technique for extracting microwave transmission line parameters from measurements made on transmission line resonators is presented in section 2.

We have successfully used the resonant technique from section 2 to measure the properties of normal conducting transmission lines and the results are presented in section 3. We have designed two independent experiments to verify the superconducting transmission line models

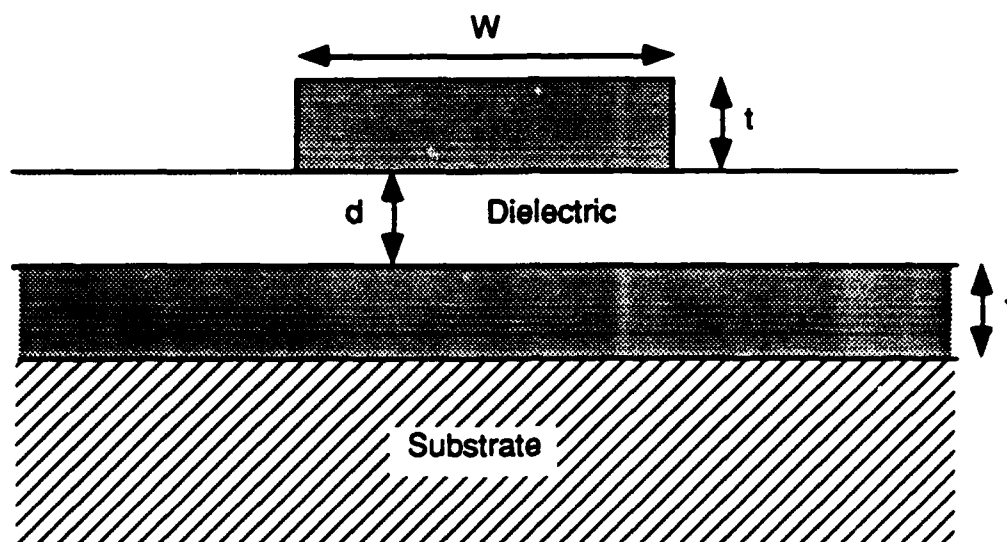


Figure 1. Microstrip (MS) Geometry

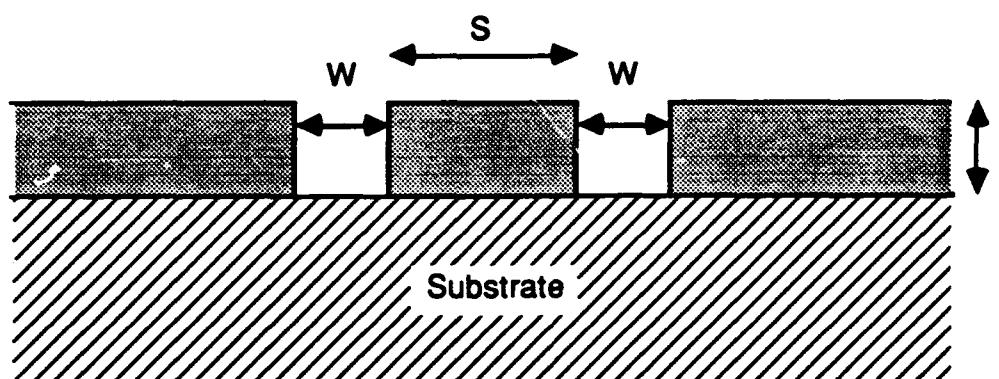


Figure 2. Coplanar Waveguide (CPW) Geometry

developed in section 2. These proposed experiments are an impedance mismatch coupled resonator and a dielectric step coupled resonator and are described in section 3. Designs for test circuits, along with associated matching networks are presented. Section 4 presents our recommendations for future work at MITRE in the area of superconducting microwave transmission lines.

## SECTION 2

### SUPERCONDUCTING TRANSMISSION LINES

The unique properties of superconducting materials can be exploited in microwave circuits to provide low-loss/dispersionless transmission lines, compact delay lines, and high-Q resonators. These applications result from fundamental differences in conductivity and field penetration between conventional metals and superconductors. For example, the surface impedance of a superconductor is several orders of magnitude more reactive than it is lossy. Also, field penetration into a superconductor is less than the classical skin depth and is essentially independent of frequency, thereby greatly reducing material dispersion in waveguides. In this section we will first examine the surface impedance of superconductors, and then present transmission line models which include this superconducting surface impedance.

#### 2.1 SUPERCONDUCTING SURFACE IMPEDANCE

Superconductivity is the name given to a remarkable state transition of a material which is characterized by the disappearance of electrical resistance and the complete expulsion of magnetic flux. The name superconductivity was coined by Kamerlingh Onnes who, in 1911, discovered that resistance of a mercury filament abruptly dropped to an immeasurably small value at a temperature of approximately 4.2 kelvin (K). The diamagnetic property of superconductivity was discovered in 1933 by Meissner and Ochsenfeld, who showed that the transition to the superconducting state involved the expulsion of magnetic flux in a superconductor. This is in contrast to a perfect conductor, which would be expected to trap magnetic flux lines in place.

The temperature at which the superconducting state transition occurs is known as the critical temperature ( $T_c$ ). The noun *superconductor* refers to a material which undergoes this state transition. A superconductor exhibits zero DC resistivity and diamagnetism at temperatures below the  $T_c$ , and the adjective *superconducting* is used to describe this condition. At temperatures above the  $T_c$ , a superconductor behaves as a *normal* metal. Today, approximately half of the metallic elements are known to be superconductors at sufficiently low temperature, as well as many compounds including the "high- $T_c$ " ceramic materials.

Superconductivity was first characterized by phenomenological theories which attempted to account for the unique diamagnetic property of superconductors. The London theory [3] assumed that the superconductor conduction mechanism could be described by a two-fluid model which consists of normal electrons and super (resistanceless) electrons, and that diamagnetism could be explained by restrictions (not violations) of Maxwell's equations. The microscopic theory of superconductivity followed in 1956 when Cooper showed that two electrons could be coupled together into a bound state (Cooper pairs) through phonon scattering of the electrons in the lattice [4]. The hypothesis that electron-phonon interaction was responsible for superconductivity helps explain why good normal conductors (e.g., gold and copper, which do

not have strong lattice vibrations) do not superconduct, while poor normal conductors are often superconductors. Cooper's result was extended to many pairs of interacting electrons to formulate the Bardeen-Cooper-Schrieffer microscopic theory of superconductivity (usually referred to as the BCS theory) [5].

The key principle of the BCS theory is that the super electrons are actually paired electrons which have condensed into a superconducting ground state, thereby resulting in a reduction of total system energy. An important feature of the superconducting ground state is that the Cooper pairs are all in the same quantum state, have the same energy, and are all described by the same wave function. This is a consequence of the paired electrons obeying Bose-Einstein statistics and; therefore, the Pauli exclusion principle (with respect to Fermions) does not apply. Thus the Cooper pairs overlap in a superconductor, with it being energetically favorable for them to have coherent (locked) phases over macroscopic distances (*i.e.*, much greater than the lattice spacing.)

The condensation of electrons out of a continuum of allowed energy values into Cooper pairs at a single energy level also gives rise to an energy gap ( $\Delta$ ) at the Fermi surface. This energy gap is orders of magnitude less than the Fermi energy, typically about one millielectron volt, compared to Fermi energies of several electron volts. The energy gap,  $\Delta$ , is the average energy per electron of a Cooper pair, relative to the continuum. The binding energy of a Cooper pair is therefore  $2\Delta$ , this being the minimum energy required to break the pair. Thus the situation in a superconductor can be thought of as analogous to a semiconductor, with both having an energy gap at the Fermi surface. When a superconductor is at finite temperatures below the  $T_c$ , thermal energy and incident radiation can break Cooper pairs. The electrons from the broken pairs are known as excited *quasiparticles*, which behave as normal electrons with well specified momenta. Since the binding energy between paired electrons is  $2\Delta$ , absorption of incident radiation is possible for field frequencies of  $\omega > 2\Delta/\hbar$  where  $\hbar$  is the reduced Planck's constant. This frequency is referred to as the gap frequency of a superconductor, typically about 1 THz. In the following paragraphs we will describe the surface impedance of superconducting materials by first presenting the complex conductivity of superconductors according to the two-fluid model, and then extend this result to include gap phenomena and temperature effects using the BCS theory.

The London theory predicts that fields (including static fields) cannot penetrate a superconductor beyond a penetration depth  $\lambda_L$  (a material parameter, typically 100 nm.) The penetration depth of a superconductor is defined as [6]

$$\lambda_L = \frac{m}{\mu_0 n_s e^2} \quad (1)$$

where  $m$  is the electron mass,  $\mu_0$  is the free space permeability,  $n_s$  is the density of the paired electrons, and  $e$  is the elementary charge. The total electron density ( $n$ ) is the sum of  $n_s$  and the normal electron density  $n_n$ . Assuming an electric field in a superconductor in the form  $E e^{j\omega t}$  where  $\omega$  is angular frequency  $\omega = 2\pi f$  (vectors are denoted by bold face variables), the London equations are given as:

$$\text{curl } J_s = -\frac{1}{\mu_o \lambda_L^2} E \quad (2)$$

$$\frac{\partial J_s}{\partial t} = \frac{1}{\mu_o \lambda_L^2} E \quad (3)$$

where  $J_s$  is the current density of the paired electrons. The total current density is the sum of  $J_s$  and the normal electron current  $J_n$ :

$$J = J_n + J_s = (\sigma_1 - j\sigma_2)E \quad (4)$$

Equation 4 shows that the superconductor current density is related to the electric field by the *complex* conductivity of the superconductor. An equivalent circuit for the impedance of an incremental section of a superconductor is depicted in figure 3.

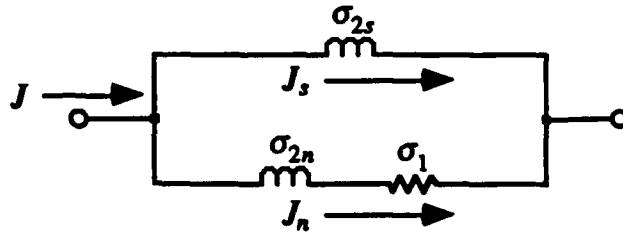


Figure 3. Superconductor Impedance Equivalent Circuit

The real and imaginary components of the complex conductivity are derived from equation 3 and a momentum relaxation equation accounting for the effect of collisions between the normal electrons. The results are given as [7]:

$$\sigma_1 = \frac{n_n e^2 \tau}{m(1 + \omega^2 \tau^2)} \quad \sigma_2 = \frac{n_s e^2}{m\omega} + \frac{n_n e^2 (\omega \tau)^2}{m\omega(1 + \omega^2 \tau^2)} \quad (5)$$

where  $\tau$  is the momentum relaxation time. Note that the real part of the conductivity depends only on the normal electrons. Therefore superconductors are only "lossless" at DC, and losses will result from changing fields due to the normal electrons present. At frequencies low enough

such that  $\omega^2 \tau^2 < 1$  (typically less than 100 GHz),  $\sigma_1$  and  $\sigma_2$  can be reduced and by substitution of equation 1 we obtain:

$$\sigma = \sigma_1 - j\sigma_2 = \sigma_n(n_n/n) - j(1/\omega\mu_0\lambda_L^2) \quad (6)$$

$$\text{where } \sigma_n = ne^2\tau/m \quad (7)$$

The normal state conductivity,  $\sigma_n$ , is related to the penetration depth and the energy gap at a temperature of absolute zero by:

$$\sigma_n = \frac{\hbar}{\pi\Delta(0)\lambda_L^2(0)} \quad (8)$$

The real and imaginary components of the conductivity can be calculated using the two-fluid model. However, the two-fluid model does not take into account energy gap effects such as electron pair splitting due to incident radiation. It has been shown that accurate calculations of the superconductor conductivity require the use of the Mattis-Bardeen theory [8] where expressions of the complex conductivity were derived from the BCS theory [9]. In general the Mattis-Bardeen theory is quite complicated, but in the extreme anomalous limit their result reduces to integral equations which can be solved numerically. These equations are given as:

$$\begin{aligned} \frac{\sigma_1}{\sigma_n} &= \frac{1}{\hbar\omega} \int_{\Delta}^{\infty} [f(E) - f(E + \hbar\omega)] g(E) dE \\ &\quad + \frac{1}{\hbar\omega} \int_{\Delta - \hbar\omega}^{-\Delta} [1 - f(E + \hbar\omega)] g(E) d(E) \end{aligned} \quad (9)$$

$$\frac{\sigma_2}{\sigma_n} = \frac{1}{\hbar\omega} \int_{\Delta - \hbar\omega, -\Delta}^{\Delta} \frac{[1 - 2f(E + \hbar\omega)] [E^2 + \Delta^2 + \hbar\omega E]}{[\Delta^2 - E^2]^{1/2} [(E + \hbar\omega)^2 - \Delta^2]^{1/2}} dE \quad (10)$$

where  $f(x)$  is the Fermi function,

$$f(x) = \frac{1}{1 + e^{x/k_B T}} \quad (11)$$

$$\text{and } g(E) = \frac{E^2 + \Delta^2 + \hbar\omega E}{\sqrt{E^2 - \Delta^2} \sqrt{(E + \hbar\omega)^2 - \Delta^2}} \quad (12)$$

The first integral of equation 9 represents thermally excited quasiparticles, while the second integral accounts for photon-excited quasiparticles and is zero below the gap frequency. Equation 10 for  $\sigma_2$  considers the paired electrons and its lower limit is taken as  $-\Delta$  at frequencies above the gap frequency ( $\hbar\omega > 2\Delta$ ). In equation 12 the signs of the square roots are such that  $g(E)$  is positive in both integrals of equation 9. The energy gap has an implied temperature dependence which can be found by solving for the root of [10, 11]:

$$\frac{\Delta(T)}{\Delta(0)} = \tanh\left[\frac{T_c}{T} \frac{\Delta(T)}{\Delta(0)}\right] \quad (13)$$

or approximated by [12]:

$$\Delta(T) = \Delta(0) \sqrt{\cos\left[\frac{\pi}{2} (T/T_c)^2\right]} \quad (14)$$

The assumption of the extreme anomalous limit is typically valid for pure elemental superconductors. The material of interest in this paper (niobium) is a London superconductor (*i.e.*, current density at a point may be described by a constant, local field.) However, the Mattis-Bardeen theory provides the best available means to calculate the complex conductivity of a superconductor [13], and this theory has been shown to exhibit good correlation with experimental results for both niobium [14, 15] and high- $T_c$  ceramic superconductors [16, 17]. Therefore, we will use the above Mattis-Bardeen equations to calculate the complex conductivity of superconducting niobium.

A computer program, written in FORTRAN, was used to numerically integrate the Mattis-Bardeen equations 9 through 13. A typical result showing the complex conductivity as a function of frequency is shown in figure 2. The curves shown are for niobium at a temperature of 4.2 K, where  $\sigma_1$  and  $\sigma_2$  are given relative to  $\sigma_n$ . Here  $\sigma_1$  varies with frequency, which is not predicted by the two-fluid model. The London theory does predict the correct  $1/\omega$  dependence of  $\sigma_2$ . At the gap frequency (approximately 720 GHz), note the precipitous decrease of  $\sigma_2$  and the corresponding rise in  $\sigma_1$ . This is a result of the incident radiation having sufficient energy to split paired electrons.

The superconducting surface impedance  $Z_s$  is calculated using Maxwell's equations with the London equations and is given by [18]

$$Z_s = \frac{j\omega\mu_o}{\sqrt{j\omega\mu_o\sigma_1 + (1/\lambda_L^2)}} \coth\left[\epsilon\sqrt{j\omega\mu_o\sigma_1 + (1/\lambda_L^2)}\right] \quad (15)$$

We can make use of Mattis-Bardeen complex conductivity by rewriting equation 6 in the form

$$j\omega\mu_o\sigma = j\omega\mu_o\sigma_1 + (1/\lambda_L^2) \quad (16)$$



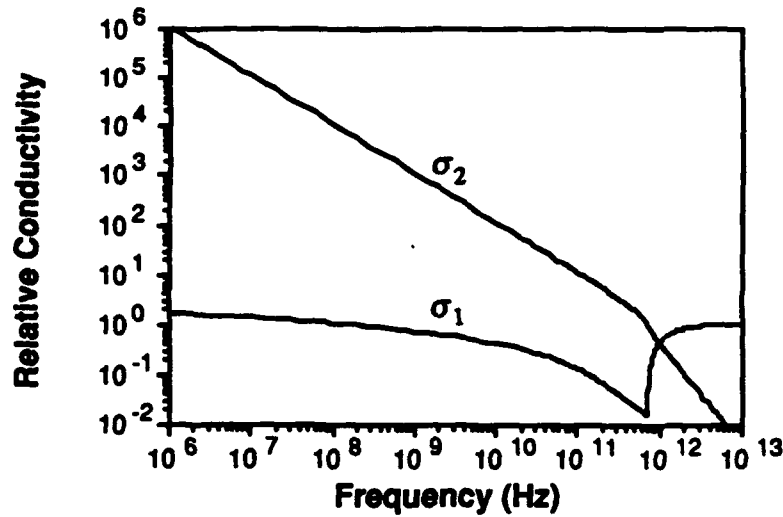


Figure 4. Relative Complex Conductivity Versus Frequency (note: the data shown is for niobium at a temperature of 4.2 K, relative to the normal state conductivity  $\sigma_n$ )

and substituting it into equation 15 to yield

$$Z_s = \sqrt{j\omega\mu_o/\sigma} \coth(t\sqrt{j\omega\mu_o/\sigma}) \quad (17)$$

where  $\sigma = \sigma_1 - j\sigma_2$  and  $t$  is the conductor metalization thickness. Figure 5 depicts the surface impedance for superconducting niobium at microwave frequencies. Note that the reactive component of the surface impedance is approximately three orders of magnitude larger than the real part. This reactive impedance is responsible for the low-loss properties of superconducting transmission lines.

Finally, we can verify the assertion that field penetration into a superconductor is less than the classical skin depth. Making use of the usual expression for skin depth

$$\delta = \sqrt{2/(\omega\mu_o\sigma_n)} \quad (18)$$

we can calculate and compare the skin depth of normal and superconducting metals. Figure 6 depicts the result, where the superconducting skin depth is much less than the normal state skin depth. This does not result in additional losses for the superconductor since the surface impedance is predominantly reactive. More importantly, the superconducting skin depth is independent of frequency, thereby greatly reducing material dispersion in waveguides.

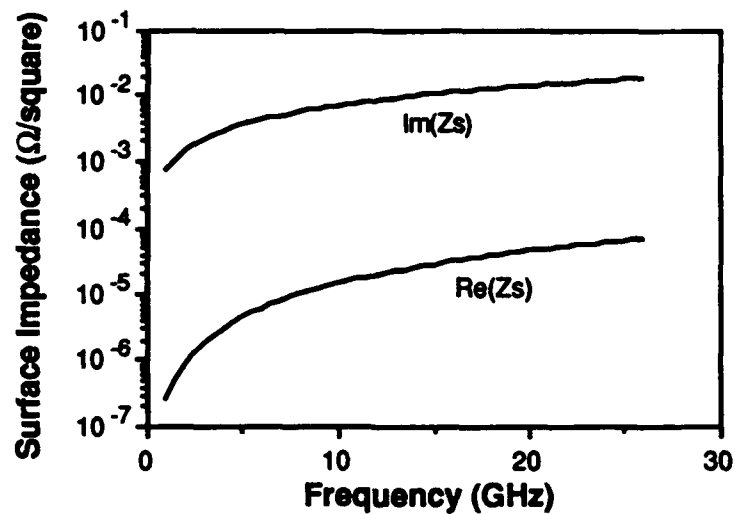


Figure 5. Superconducting Surface Impedance Versus Frequency (note: the data shown is for niobium at a temperature of 4.2 K. The normal state conductivity  $\sigma_n$  is  $15.7 \times 10^6$  S/m)

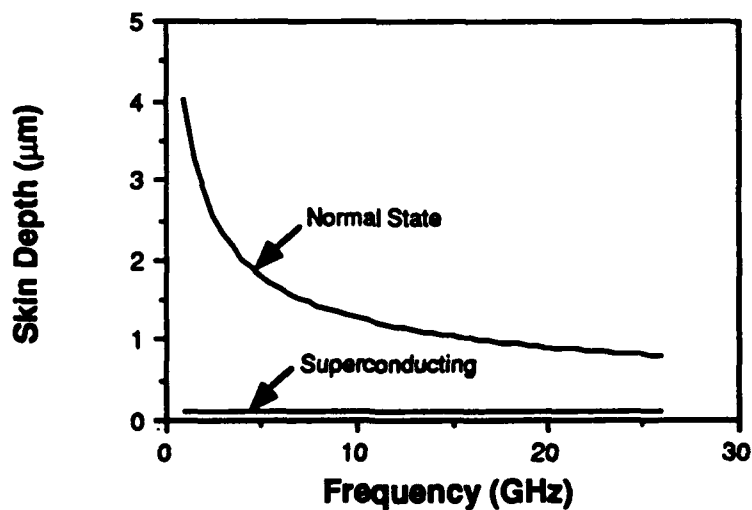


Figure 6. Superconducting and Normal Skin Depth Versus Frequency (note: the data shown is for niobium where  $\sigma_n = 15.7 \times 10^6$  S/m)

## 2.2 TRANSMISSION LINE MODELS

The physics of wave propagation on a superconducting transmission line are the same as that for normal metal waveguides. However, it was shown in the previous section that a superconductor has a fundamentally different surface impedance at microwave frequencies, where  $Z_s$  is orders of magnitude more reactive than it is lossy. This complex  $Z_s$  is calculated from the superconducting complex conductivity, which is also related to the field penetration ( $\lambda_L$ ) in the superconductor by equation 16 above. Furthermore, losses on a superconducting transmission line are proportional to the square of frequency, in contrast to the conventional surface resistance varying as the square root of frequency. It is necessary to include all of these effects in order to accurately model superconducting transmission lines. Fortunately, this can be conveniently accomplished through the use of the complex surface impedance  $Z_s$ , calculated from the superconductor complex conductivity, in the transmission line equations from the literature.

General transmission line theory defines the propagation factor  $\gamma$  which describes the attenuation and phase response of a transmission line. The propagation factor is given by

$$\gamma(f) = \alpha(f) + j\beta(f) \quad (19)$$

where  $\alpha$  and  $\beta$  are the attenuation and phase "constants," respectively. The use of the word "constant" is misleading since  $\alpha$  and  $\beta$  typically vary with frequency  $f$ . The propagation factor is defined in terms of the transmission line's distributed series impedance ( $Z$ ) and shunt admittance ( $Y$ ), which also define the characteristic impedance ( $Z_o$ ) of the transmission line. These relationships are given in equations 20 and 21.

$$\gamma = \sqrt{ZY} \quad (20)$$

$$Z_o = \sqrt{Z/Y} \quad (21)$$

The distributed series impedance and shunt admittance are functions of the transmission line geometry, and are given by

$$Z = j2\pi f\mu_o g_1 + Z_s(f)g_2 \quad (22)$$

$$Y = 2\pi f\epsilon_o (j\epsilon_{re} + \epsilon_r \tan \delta) / g_1 \quad (23)$$

In these equations  $\epsilon_o$  is the free space permittivity,  $\epsilon_r$  is the relative permittivity of the dielectric,  $\epsilon_{re}$  is a geometry dependent effective permittivity, and  $\tan \delta$  is the loss tangent of the transmission line dielectric material. The factors  $g_1$  and  $g_2$  account for transmission line geometry, allowing the above equations to be completely general.

The analysis of planar transmission lines (e.g., MS and CPW) is difficult because they cannot support a pure transverse electromagnetic (TEM) wave. This is a result of fringing electric field lines experiencing an inhomogeneous dielectric, leading to discontinuities in the field which cause contributions from longitudinal components. However, at low frequencies a quasistatic solution can be obtained by assuming that the lowest-order mode is approximately a TEM wave. This quasi-TEM approach is manifested in equation 23 as the effective permittivity  $\epsilon_{reo}$ , which is an average of the dielectric material and free space. Closed form expressions for the effective permittivity in MS is given by [19]

$$\epsilon_{reo} = \frac{1}{2}(\epsilon_r + 1) + \frac{\frac{1}{2}(\epsilon_r - 1)}{\sqrt{1 + 12d/W}} - \frac{(\epsilon_r - 1)(t/d)}{4.6\sqrt{W/d}} \quad \text{for } W/d \geq 1 \quad (24)$$

$$\epsilon_{reo} = \frac{1}{2}(\epsilon_r + 1) + \frac{\frac{1}{2}(\epsilon_r - 1)}{\sqrt{1 + 12d/W}} + 0.02(\epsilon_r - 1)(1 - W/d)^2 - \frac{(\epsilon_r - 1)(t/d)}{4.6\sqrt{W/d}} \quad \text{for } W/d < 1 \quad (25)$$

In these expressions  $W$  is the MS width,  $t$  is the metalization thickness, and  $d$  is the dielectric thickness. These are pictorially shown in figure 1. Note that these expressions have no frequency dependence, hence the notation  $\epsilon_{reo}$ . With increasing frequency, longitudinal field components become significant, causing the fields to become more concentrated in the dielectric and; thereby, increasing the effective permittivity. This results in modal dispersion, which is especially critical for superconducting transmission lines which have increased bandwidth by virtue of their reduced losses [20-22]. This modal dispersion can be expressed by an empirical formula as [23, 24]

$$\frac{\beta}{\beta_o} = \sqrt{\epsilon_{re}(f)} = \frac{\sqrt{\epsilon_r} - \sqrt{\epsilon_{reo}}}{1 + 4F^{-1.5}} + \sqrt{\epsilon_{reo}} \quad \text{where} \quad (26)$$

$$F = f\sqrt{\mu_o\epsilon_o}4d\sqrt{\epsilon_r - 1}\left\{0.5 + [1 + 2\ln(1 + W/d)]^2\right\} \quad (27)$$

Finally, the MS geometry dependent factors  $g_1$  and  $g_2$  are given in equations 28 through 34 [25].

$$g_1 = \frac{1}{2\pi} \ln \left[ \frac{8d}{W_e} + 0.25 \frac{W_e}{d} \right] \quad \text{for } W/d \leq 1 \quad (28)$$

$$g_1 = \left\{ \frac{W_e}{d} + 1.393 + 0.667 \ln \left[ \frac{W_e}{d} + 1.444 \right] \right\}^{-1} \quad \text{for } W/d > 1 \quad (29)$$

$$\frac{W_e}{d} = \frac{W}{d} + \frac{1.25}{\pi} \frac{t}{d} \left[ 1 + \ln \frac{4\pi W}{t} \right] \quad \text{for } W/d \leq \frac{1}{2\pi} \quad (30)$$

$$\frac{W_e}{d} = \frac{W}{d} + \frac{1.25}{\pi} \frac{t}{d} \left[ 1 + \ln \frac{2d}{t} \right] \quad \text{for } W/d > \frac{1}{2\pi} \quad (31)$$

$$g_2 = \frac{1}{2\pi d} \left\{ 1 - \left[ \frac{W_e}{4d} \right]^2 \right\} \left\{ 1 + \frac{d}{W_e} + \frac{d}{\pi W_e} \left[ \ln \frac{4\pi W}{t} + \frac{t}{W} \right] \right\} \quad \text{for } \frac{W}{d} \leq \frac{1}{2\pi} \quad (32)$$

$$g_2 = \frac{1}{2\pi d} \left\{ 1 - \left[ \frac{W_e}{4d} \right]^2 \right\} \left\{ 1 + \frac{d}{W_e} + \frac{d}{\pi W_e} \left[ \ln \frac{2d}{t} - \frac{t}{d} \right] \right\} \quad \text{for } \frac{1}{2\pi} < \frac{W}{d} \leq 2 \quad (33)$$

$$g_2 = \frac{\left\{ \frac{W_e}{d} + \frac{\frac{W_e}{\pi d}}{\frac{W_e}{2d} + 0.94} \right\} \left\{ 1 + \frac{d}{W_e} + \frac{d}{\pi W_e} \left[ \ln \frac{2d}{t} - \frac{t}{d} \right] \right\}}{d \left\{ \frac{W_e}{d} + \frac{2}{\pi} \ln \left[ 2\pi e \left( \frac{W_e}{2d} + 0.94 \right) \right] \right\}^2} \quad \text{for } 2 < \frac{W}{d} \quad (34)$$

A computer program, written in FORTRAN, was used to calculate the propagation characteristics of superconducting microstrips to illustrate some of the properties of superconducting transmission lines, and more importantly serve as a base line for developing an experiment to verify these properties. Figure 7 shows the attenuation of a 10  $\mu\text{m}$  MS line, a dielectric thickness of  $d = 0.1 \mu\text{m}$ , and fabricated from superconducting niobium. In the figure, the loss of the superconducting MS is compared with a normal state MS which is representative of either copper or aluminum metalization. Note that the loss for the superconducting MS is approximately four orders of magnitude less than that predicted for the normal state MS, albeit the superconducting losses are increasing as the square of frequency.

Figure 8 depicts the propagation constant (normalized to the free space propagation constant  $\beta_0$ ) of a superconducting MS as a function of the dielectric thickness. This simulation illustrates an interesting feature of superconducting transmission lines which can be exploited to build compact delay lines. In the figure, note that the propagation constant is inversely proportional to the dielectric thickness, and actually becomes greater than the relative dielectric constant of the substrate (here  $\epsilon_r = 4$ ). This effect is due to the kinetic inductance of the paired electrons, as manifested through the superconducting complex conductivity. An essential requirement for this effect to be exhibited is the close physical proximity of two superconductors, in this case the MS conductor and its ground plane.

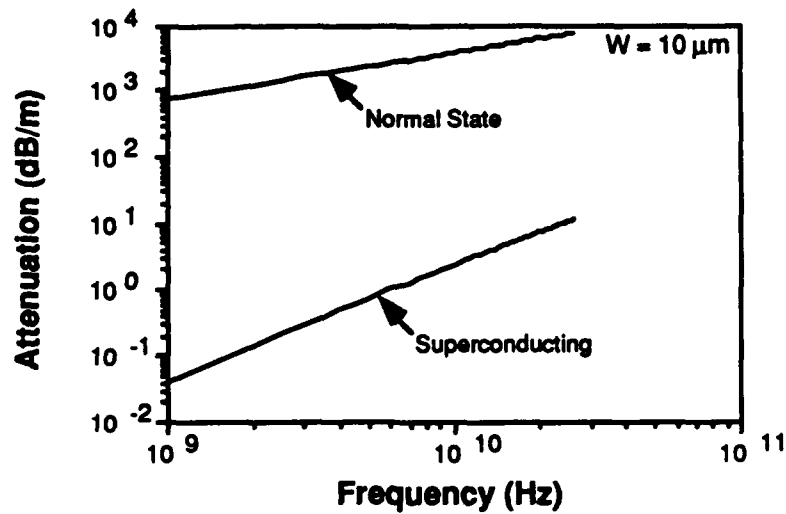


Figure 7. Attenuation as a Function of Frequency for a Microstrip Transmission Line (note: the simulation shown is for  $W = 10 \mu\text{m}$ ,  $d = 0.1 \mu\text{m}$ ,  $t = 0.1 \mu\text{m}$ , and  $\sigma_n = 15.7 \times 10^6 \text{ S/m}$ )

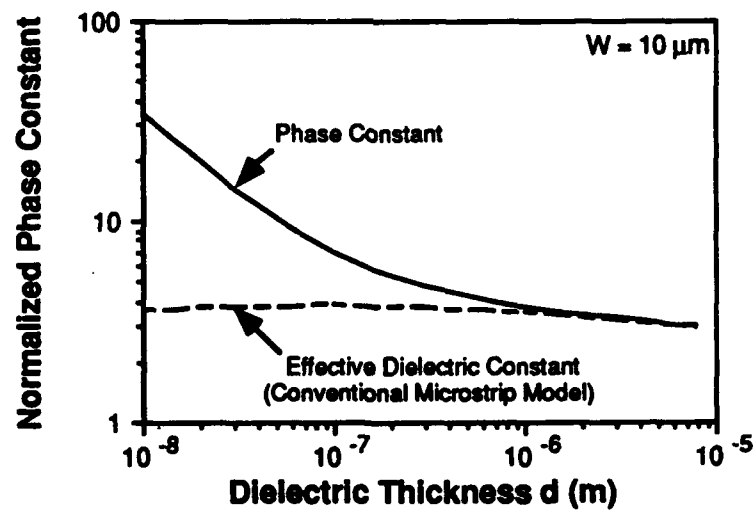


Figure 8. Microstrip Phase Constant Versus Dielectric Thickness

Figure 9 depicts the characteristic impedance  $Z_0$  for a superconducting MS as a function of dielectric thickness. Three MS widths are shown. As described in the next section, the data in figure 9 was used to choose the impedance of a MS resonator for an experimental verification of the theories presented in this section.

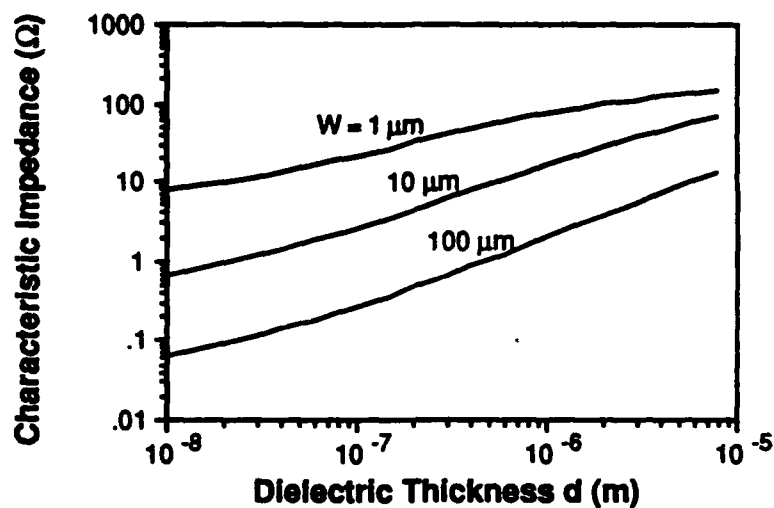


Figure 9. Microstrip Characteristic Impedance Versus Dielectric Thickness

### 2.3 TRANSMISSION LINE CHARACTERIZATION TECHNIQUES

In order to verify our models, a method for measuring the complex propagation factor,  $\gamma$ , of a microwave transmission line is required. The complex propagation factor consists of two parts. The imaginary part,  $\beta$  is proportional to the phase velocity on the line. The real part,  $\alpha$ , is the attenuation constant of the line. A resonant technique should be employed to perform these measurements due to the increased accuracy of this technique as opposed to straight transmission line S parameter measurements [19]. Reflection ( $S_{11}$ ) measurements or transmission ( $S_{21}$ ) measurements on transmission line resonators can both be performed to determine the complex propagation constant of a transmission line.

The measurement of  $\beta$  requires two resonators of different lengths in order to account for the effects of reactive discontinuities on the effective resonator length. The measurement of  $\alpha$  requires only one resonator. The measurement of  $\alpha$  on the second resonator gives us increased measurement accuracy as the two results can be averaged.

In order to perform measurements on a resonator, the resonator must be coupled to the measurement system. This coupling must be loose so that the resonance condition is not disturbed. The coupling to the resonator must not be so loose that the reflected or transmitted signal from the resonator cannot be measured. As a general rule, about 20 dB of coupling is desired, measured away from the resonant frequency. The most widely used coupling scheme for MS and stripline resonators is to end couple through a capacitive gap. This is due to the existence of accurate models for these gaps, and the minimal effects on resonator performance. For CPW resonators, the most widely used coupling method is a feed line normal to the resonator, in the center. End coupling of CPW resonators has also been demonstrated [26].

A resonance condition exists in a transmission line section when a standing wave pattern exists which satisfies the boundary conditions at the end of the line. If the ends of the resonator are open circuited or short circuited, and the resonator is a multiple of  $1/2$  wavelength long, a resonance condition will exist. MS resonators are almost always implemented as open circuit sections because no via holes are necessary to achieve an open circuit. With CPW, short circuit and open circuit resonators are both easily realizable. Of the many CPW resonators described in the literature, all except one are short circuited sections. However, research by Gopinath [27] claims that open circuited CPW resonators have lower radiation losses.

The procedure for extracting transmission line parameters from resonance measurements is as follows. First, two resonators of different lengths, but identical in all other ways including coupling circuits must be fabricated. Both  $\alpha$  and  $\beta$  can then be obtained from automatic network analyzer  $S_{11}$  or  $S_{21}$  measurements on these resonators.

The measurement of  $\beta$  involves measuring the resonant frequencies of the two resonators  $f_1$  and  $f_2$ . For a reflection measurement, a minimum value of  $S_{11}$  is obtained at the resonant frequency. For a transmission measurement  $S_{21}$  reaches a maximum value at the resonant frequency. All of the discontinuities associated with the resonator and coupling circuits can be



represented as an effective reactance, which in turn can be modeled as a change in the line length of the resonator which is referred to as  $\Delta l_d$ . When the effective line length is a multiple of  $1/2$  wavelength, a resonance occurs. The resonant frequency, line length and effective dielectric constant are related by the equation:

$$l_1 + \Delta l_d = \frac{n_1 c}{2f_1 \sqrt{\epsilon_{re}}} \quad (35)$$

where  $l_1$  is the physical length of the first resonator,  $n_1$  is an integer,  $c$  is the speed of light in vacuum, and  $\epsilon_{re}$  is the effective dielectric constant of the line. Similarly for the second resonator:

$$l_2 + \Delta l_d = \frac{n_2 c}{2f_2 \sqrt{\epsilon_{re}}} \quad (36)$$

These two equations can be solved simultaneously for  $\epsilon_{re}$  and  $\Delta l_d$ .  $\beta$  is related to  $\epsilon_{re}$  by the simple relation:

$$\beta = \omega \sqrt{\mu_0 \epsilon_0 \epsilon_{re}} \quad (37)$$

where  $\omega$  is the resonant angular frequency. The measurement assumes that there is no dispersion (i.e., the transmission line parameters, and  $\Delta l_d$  are the same at both resonant frequencies). This will not be a problem if the two different resonators lengths are fairly close to each other (within  $1/10$ th of a wavelength at the resonant frequency) or if the resonator lengths differ by a multiple of  $1/2$  wavelength at the frequency of interest giving them approximately the same resonant frequency.

The main source of error in the attenuation measurements is radiation losses associated with the open end discontinuities of the resonator. There are two solutions to this problem. The first is to shield the resonator in a hollow metallic waveguide with a cutoff frequency above the desired measurement range. This will cause the resonator radiation to couple to evanescent modes in the waveguide which are reflected back into the resonator and are not lost. The second method for avoiding errors due to radiation is to use existing models for the radiation at open ends and subtract this from the measured loss. Radiation models for MS open ends and coplanar open ends exist in the literature [28]. Although we are concentrating on MS in this paper, it is important to note that this resonant technique can be used to analyze any type of transmission line provided the radiation losses can be accounted for. No closed form approximations exist to model the radiation effects in CPS, however an electromagnetic (EM) simulator could be used to model these effects. The radiation problem is greatly reduced in stripline geometry which does not have higher order radiation modes. The stripline technique is the most widely used to date in the measurement of the very small attenuation constants associated with superconducting transmission lines.

The quality factor ( $Q$ ) of a resonator is defined as the product of the resonant frequency and the energy stored in the resonator, divided by the average power loss in the resonator. For the  $\alpha$

measurement the unloaded  $Q$  of each resonator must be measured. The unloaded  $Q$  is the  $Q$  associated only with losses in the resonator. The unloaded  $Q$  of a resonator consists of three components,  $Q_c$  associated with conductor losses,  $Q_d$  associated with dielectric losses, and  $Q_r$  associated with radiation losses. The total unloaded  $Q$  is related to these components by

$$\frac{1}{Q} = \frac{1}{Q_c} + \frac{1}{Q_d} + \frac{1}{Q_r} \quad (38)$$

The loaded  $Q$  factor includes losses associated with the external coupling circuit. Each resonator used in the  $\beta$  measurement will yield an independent measure of  $Q$  near its resonant frequency. There are two methods for doing this. Both methods will de-embed the effects of the coupling circuit, but not any radiation effects associated with the resonator itself. The two attenuation measurement techniques were proposed by Kajfez [29] and Ginzton [30]. These methods are described below.

The first method is proposed by Ginzton. This method can be utilized on both reflection or transmission measurements. For a transmission measurement, the frequencies on either side of resonance which have transmission 3 dB below the resonance level are found and labeled  $F_a$  and  $F_b$ . The loaded  $Q$  is then given by the equation

$$Q_l = \frac{F_r}{F_a - F_b} \quad (39)$$

where  $F_r$  is the resonant frequency. The coupling coefficient,  $k$  associated with the transmission resonator is given by

$$k = \frac{|S_{21 \max}|}{2(1 - |S_{21 \max}|)} \quad (40)$$

Once the coupling coefficient is determined, the unloaded  $Q$  can be obtained from

$$Q = Q_l(1 + 2k) \quad (41)$$

The use of Ginzton's method for reflection measurements is slightly more complicated because the return loss at resonance is usually within 3 dB of the return loss away from resonance. Ginzton has chosen to use Voltage Standing Wave Ratio (VSWR) measurements to find the half power points on the resonance curve. The frequencies at the half power points on the VSWR curve are defined as  $F_a$  and  $F_b$ . The VSWR at these points is given by the expression:

$$\text{VSWR}_{a,b} = \frac{2 + y^2(1 + z^2) + \sqrt{4 + y^2(1 + z^4) - 2zy^2(4 - zy^2)}}{2y(1 + z)} \quad (42)$$

In this procedure three new parameters,  $x$ ,  $y$ , and  $z$  are defined using VSWR measurements.  $y$  is defined as  $1/(\text{VSWR at resonance})$ ,  $x$  is given by  $1/(\text{VSWR away from resonance})$  and  $z$  is  $x/y$ . The unloaded  $Q$  of the resonator is given by

$$Q = F_r / (F_b - F_a). \quad (43)$$

The second method for finding the unloaded  $Q$  of a resonator is a graphical procedure proposed by Kajfez [30] which utilizes reflection measurements. This procedure relies on the fact that the reflection response ( $S_{11}$ ) of a resonator traces approximately a circle on the Smith Chart as the frequency is swept through resonance. This is illustrated in figure 10. The point on the circle closest to the center of the Smith Chart is the resonant frequency and this is defined as point 3. The diameter of the circle ( $D$ ) is a function of the coupling efficiency. Points 1 and 2 and their corresponding frequencies  $f_1$  and  $f_2$  are found by picking two points on the circle some arbitrarily small angle  $\phi$  away from resonance. These two points on the Smith Chart are located at the positions:

$$\Gamma_{1,2} = \left(\frac{|\Gamma_r|+1}{2}\right)e^{i\theta} + \left(\frac{|\Gamma_r|-1}{2}\right)e^{i(\theta \pm 2\phi)} \quad (44)$$

The loaded  $Q$  can now be found by the expression:

$$Q_l = \frac{f_r}{f_2 - f_1} \tan \phi \quad (45)$$

The coupling coefficient  $k$  can be found from:

$$k = \frac{1 - |\Gamma_r|}{1 + |\Gamma_r|} = \frac{D}{2 + D} \quad (46)$$

and the desired unloaded  $Q$  is given by

$$Q = Q_l(1+k). \quad (47)$$

The factor of two which is found in equation 41 and not in equation 47 was removed because this is a reflection measurement and only one port is involved.

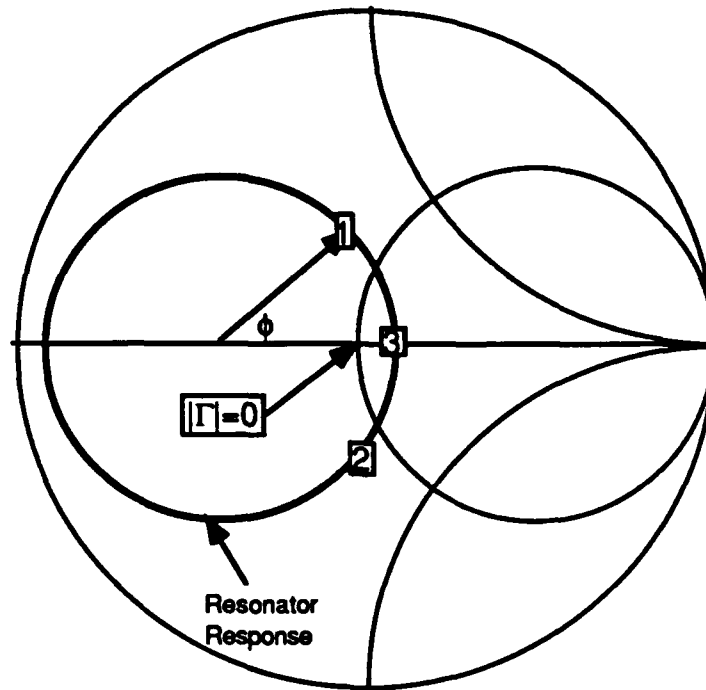


Figure 10. Reflection Coefficient of a Resonator Plotted on the Smith Chart

The attenuation constant can be determined from the phase constant,  $\beta$ , and the unloaded  $Q$  of the resonator as

$$\alpha = \frac{\beta}{2Q} \quad (48)$$

It is important to remember that this attenuation constant includes the effects of any radiation from discontinuities in the resonator itself. Due to the resistance free properties of the superconducting transmission lines, the attenuation constant will be extremely small, resulting in very high  $Q$  resonators.

## SECTION 3

### PROPOSED EXPERIMENTS

In this section we describe experiments which have designed in order to measure the transmission line parameters of superconducting transmission lines using the resonant technique described in section 2.3.

#### 3.1 NORMAL CONDUCTOR RESONATOR MEASUREMENTS

In order to use the techniques described in section 2.3, we must be able to accurately measure the resonant frequency and quality factor of a transmission line resonator. In order to determine the accuracy of our measurement system and simulation tools, preliminary simulations and measurements on non-superconducting MS resonators fabricated on duroid substrates were performed. The resonators and feed circuits were modeled using both Supercompact and Sonnet software's EM simulator. In order to minimize fabrication costs, two resonators were fabricated on the same substrate. Reflection type resonators were chosen so that a minimum of connectors would be required.

The circuit used in this experiment is shown in figure 11. The circuit consists of two MS resonators with different lengths and identical feed structures. This structure was chosen because it can be modeled using both Supercompact and Sonnet, and can be packaged in our existing test fixture. Measurements were made using a Wiltron 360 automatic network analyzer. Results from each of the simulations and the experiment are summarized in table 1. Note that the Sonnet simulations are designated "EM." The resonant frequencies predicted by Sonnet agreed very well with the measurement. The Supercompact simulation was considerably less accurate. Neither simulation was accurate in predicting the Q of the resonators.

Sonnet's EM simulator has an option of using corner fill to subsection the rectangles, and they recommend using this feature whenever capacitive coupling is to be analyzed. With corner fill, Sonnet was able to predict the resonant frequency very accurately. Supercompact does provide a close approximation, and is much quicker to calculate data. Sonnet takes about ten minutes per frequency point calculation, while Supercompact takes about two seconds. Neither of the simulators was able to predict the Q of the resonator closely. This is probably due to surface roughness and impurities in the metalization. The difference between the simulated Qs is due to the fact that Supercompact does not model the radiation from open end discontinuities. The difference between the Supercompact and Sonnet result provides an indication of the magnitude of the error caused by radiation effects.

The results of this preliminary study were extremely encouraging. The measurements of duroid MS resonators confirmed the effectiveness of our experimental technique. We have gained confidence in Sonnet software's ability to accurately simulate resonator circuits. This will

be important as the design of our superconducting resonator circuits are based on simulations performed with Sonnet.

Measurements of actual superconducting resonators will be considerably more difficult to achieve. This is due to the very low losses of superconductors which will result in large resonator  $Q$ s. At DC, a superconductor has zero resistance, however at RF frequencies the resistance increases as the square of the frequency. At microwave frequencies (1 - 20 GHz) the surface resistance of superconducting niobium is about three orders of magnitude smaller than copper. The highest reported  $Q$  for a superconducting resonator is  $5 \times 10^4$  [31], although our niobium resonators should have  $Q$  factors much lower than this due to surface roughness and impurities. With the 100-KHz accuracy of our Wiltron network analyzer we can measure  $Q$  factors up to  $10^5$ . The HP 8510 network analyzer has an HP8341 synthesizer with 1 Hz accuracy which will resolve a  $Q$  factor of  $10^{10}$  at 10 GHz.

A potential problem which became obvious during the normal conductor measurements is the low value of return loss, even at the resonant frequency. The copper/duroid resonators had a return loss of about 5 dB at resonance which was very easy to resolve from other noise associated with the system. If the reflection losses of superconducting resonators are two orders of magnitude lower than the copper resonators, it may be impossible to detect the resonance above the noise floor of the system. This problem could be avoided by using a transmission measurement, optimizing the coupling, providing matching circuits, and by de-embedding inside the test fixture through attachment of the calibration standards within the dewar. We did not test a transmission resonator made from normal conductors because we have shown that we can accurately simulate resonator performance and it was not necessary to fabricate another circuit.

### 3.2 SUPERCONDUCTING TRANSMISSION LINE GEOMETRY

As shown in section 2, the effective dielectric constant of a superconducting transmission line can be made greater than the dielectric constant of the material used for the transmission line. This will only occur if the kinetic inductance effects of the superconducting material are much greater than the normal inductance effects of the transmission line. To accomplish this, a majority of the magnetic field must be contained within the superconductor. In order to confine the magnetic fields to the superconductor, and not the dielectric, the two conductors of any TEM or quasi-TEM transmission line must be extremely close.

This restriction of conductor spacing limits the types of practical lines that can be fabricated with existing photolithography. In superconducting MS, kinetic inductance does not have a significant effect on the propagation constant unless the dielectric thickness is on the order of 0.1  $\mu\text{m}$  or less. Fabrication of 0.1- $\mu\text{m}$   $\text{SiO}_2$  dielectric layers is routinely accomplished without pinholes which would short a MS line. CPW and CPS transmission lines are not practical for this application due to the extremely small gaps that would have to be photolithographically defined. For this reason we have chosen to concentrate our study exclusively on MS transmission lines.

The use of a very thin dielectric imposes some restrictions on the measurement techniques available for this study. According to our models, MS lines of reasonable width have very low characteristic impedances. A 50- $\mu\text{m}$  wide line with a 0.1- $\mu\text{m}$  dielectric has a characteristic impedance of 0.5 ohms. A 5- $\mu\text{m}$  wide line has a characteristic impedance of 4 ohms. Lines smaller than this which extend for a few mm are not practical to fabricate with existing photolithography technology.

Coupling to thin MS lines from a 50-ohm coaxial measurement system is a challenging engineering problem. In the duroid substrate experiment, coupling through a capacitive gap was used. This technique is not possible with thin dielectric MS as shown in figure 12. The field lines extend at most 1  $\mu\text{m}$  away from the edge of a MS with 0.1- $\mu\text{m}$  dielectric thickness [32]. A gap any bigger than 1  $\mu\text{m}$  will provide very little coupling. This was verified with Sonnet software's EM simulator. In the simulation, a 100- $\mu\text{m}$  wide MS line on a 0.1- $\mu\text{m}$  substrate was coupled to another line through a 1- $\mu\text{m}$  gap. The coupling was less than -60 dB. The limits of photolithography prevent us from making a gap small enough to provide any significant coupling to a resonator.

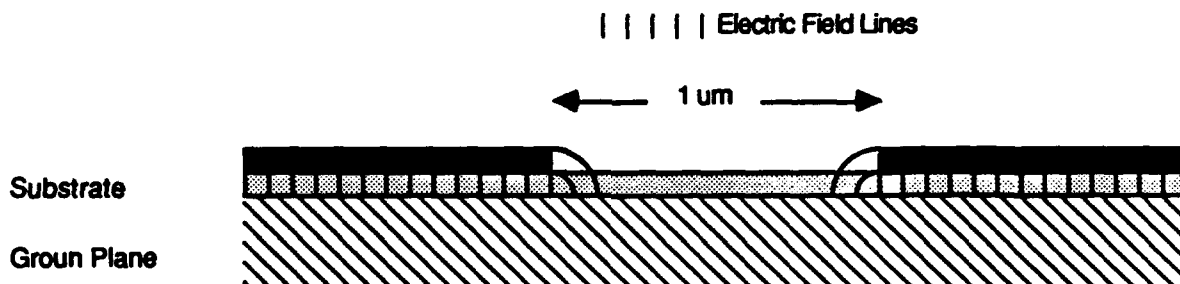


Figure 12. Gap Coupling in Thin Dielectric Microstrip

Any coupling scheme that is used will need to account for a large mismatch in impedance as well as an extreme change in line geometry. At microwave frequencies, our goal will not be a perfect match since this will be extremely difficult to achieve. Instead the goal of the coupling scheme should be to transfer enough power to the MS line to allow us to measure the desired quantities (resonant frequency and Q factor). In the measurement technique outlined above, both reflection and transmission resonator methods are presented. Reflection measurements will not be practical for kinetic inductance MS. Due to line discontinuities most of the incident power will be reflected back to the source before it gets to the resonator. A reflection measurement will have to discriminate a small resonance from a large reflected signal. For this reason transmission measurements such as Ginzton's method should be employed to characterize superconducting transmission lines.

After abandoning the gap coupling technique, we have developed two methods for achieving the desired coupling. The two methods are impedance mismatch coupling and dielectric step coupling. Impedance mismatch coupling is simpler to implement, but produces reduced accuracy. Impedance mismatch coupling is described below and the stepped dielectric coupled resonator is described in section 3.3.

Impedance mismatch coupling utilizes the impedance mismatch between the measurement system and the resonator as a loose coupling mechanism. This technique has been successfully utilized by Pond [2] in a measurement of kinetic inductance MS lines. This method would involve measurements on relatively wide (10 - 100  $\mu\text{m}$ ) lines which would be coupled by a precision coax to MS adapter such as a Wiltron beaded K connector as shown in figure 13.

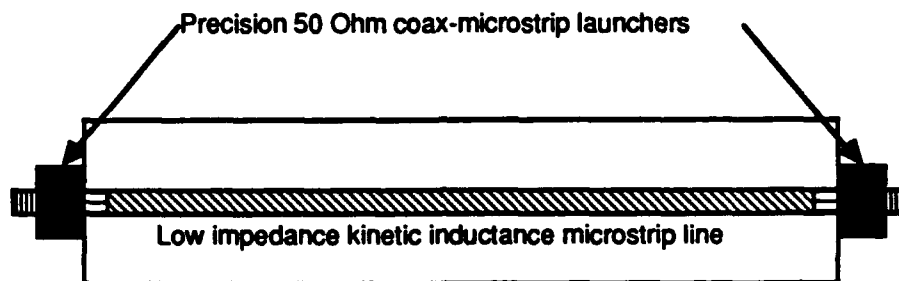


Figure 13. Impedance Mismatch Coupled Resonator

The impedance mismatch technique described above will have sufficient accuracy for our purposes. The length of the resonator is defined by the positioning of the MS launchers. The measurement technique relies on being able to accurately define the length of the resonator. Recall that for the phase velocity ( $\beta$ ) measurement, two resonators of different lengths are required. The two simultaneous equations to be solved for the effective dielectric constant are given by 2.35 and 2.36 where  $l_1$  is the physical length of the first resonator,  $n_1$  is an integer,  $c$  is the speed of light in vacuum, and  $\epsilon_{re}$  is the effective dielectric constant of the line. Similarly for the second resonator  $l_2$  is the length and  $n_2$  is its resonant mode number. These two equations can be solved simultaneously for  $\epsilon_{re}$  and  $\Delta l_d$ . The equation for  $\epsilon_{re}$  is given by:

$$\epsilon_{re} = \left\{ \frac{c}{2(l_1 - l_2)} \left[ \frac{n_1}{f_1} - \frac{n_2}{f_2} \right] \right\}^2 \quad (49)$$

Errors occur due to inaccuracies in the measurement of  $l_1 - l_2$ . The accuracy of this measurement can be greatly improved by choosing  $n_1$  different from  $n_2$ . If  $n_1 = 1$  and  $n_2 = 2$



(i.e., the first resonator is  $1/2$  wavelength long and the second resonator is a full wavelength long) then  $l_1 - l_2$  is a much larger value and the small error in resonator length due to the launcher is not as significant. Using different resonant modes will improve the accuracy of this measurement significantly. This will be demonstrated later in the next section.

One potential problem with the impedance mismatch technique is that the extremely thin substrate will puncture easily when the connector is attached. If the substrate is punctured, the transmission line could become shorted. Pond has avoided this problem by cutting out a small hole in the ground plane in the area where the connector is to be attached. At 500 MHz this discontinuity lowers the coupling coefficient by about 1 dB. It is our goal to make measurements at frequencies as high as 10 GHz. In order to avoid undesired radiation or reflections, the hole in the ground plane should be kept much smaller than a wavelength. At 10 GHz, a 2-mm hole will be less than  $1/7$ th of a wavelength on a  $\text{SiO}_2$  substrate. This should be small enough that any errors can be removed with the measurement techniques described above.

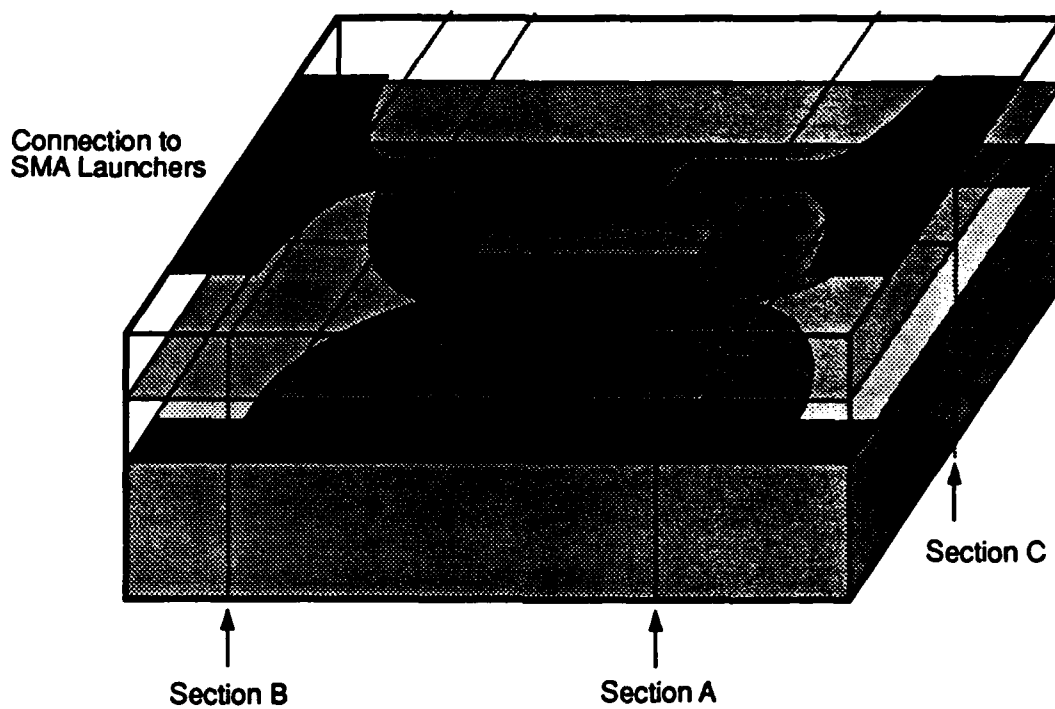
The final design for the impedance mismatch resonator measurement circuit will consist of two MS lines of 100- $\mu\text{m}$  width, deposited on a 0.1  $\mu\text{m}$  thick substrate. The two resonator lengths are 1.1 and 0.55 cm and should resonate at approximately 10 GHz.

### 3.3 DIELECTRIC STEP COUPLED RESONATOR

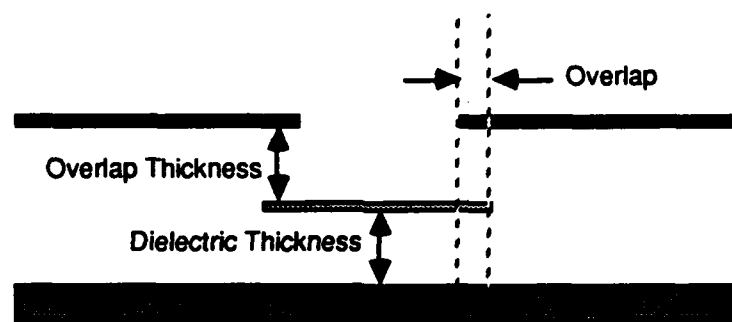
Due to the potential risk involved with the impedance mismatch coupled resonator, and its limited accuracy, we have designed a second resonator coupling mechanism. This coupling mechanism is described in section 3.3.1. If an impedance step is not used, it becomes necessary to match a low impedance MS to a high impedance coax through a transformer of some sort. The transformer must have a flat broad band frequency response near the resonant frequency we are trying to measure. A sinusoidal or a Dolph-Chebyshev impedance taper will be suitable for this purpose [33]. Section 3.3.2 describes a method for realizing this transformer. In section 3.3.3 we present the results of simulations which were performed to insure that substrate resonances in our circuits would not interfere with our measurements.

#### 3.3.1 Resonator Design

In this section, the dielectric step coupled resonator is described. Many possible coupling methods were simulated using Sonnet software. It was found that coupling through a step in line width or through an abrupt CPW-MS transition would not produce a measurable level of coupling. It was found that the best results were obtained by a change in dielectric thickness. If we couple a line with a dielectric thickness of 0.2  $\mu\text{m}$  to a line with a common ground plane and a dielectric thickness of 0.1  $\mu\text{m}$ , the desired loose coupling is achieved. This overlap coupling is shown in figure 14.



(a) Perspective View



(b) Section C Cross-Sectional View

Figure 14. Geometry of a Dielectric Step Coupled Microstrip Resonator

A simulation of dielectric step coupling was performed using Sonnet software. Two different width resonators were simulated. The resonator widths are 10 and 100  $\mu\text{m}$ , and the dielectric thickness and overlap thickness is 0.1  $\mu\text{m}$  in both cases. The overlap length is 100  $\mu\text{m}$  for both resonators. Using our models, the resonant frequency is designed to be 10 GHz. Figure 15 shows a simulation of the frequency response of two different width, 0.57-cm long resonators coupled to their test ports by dielectric steps. The 100- $\mu\text{m}$  wide resonator has a higher Q factor but is not coupled as well as the 10- $\mu\text{m}$  resonator. These simulations show that dielectric step coupled resonators will produce the desired response. Based on these simulations we determined that the optimum overlap thickness is equal to the dielectric thickness. The dielectric thickness was chosen as 0.1  $\mu\text{m}$  because this is the smallest thickness which can be deposited without pinholes.

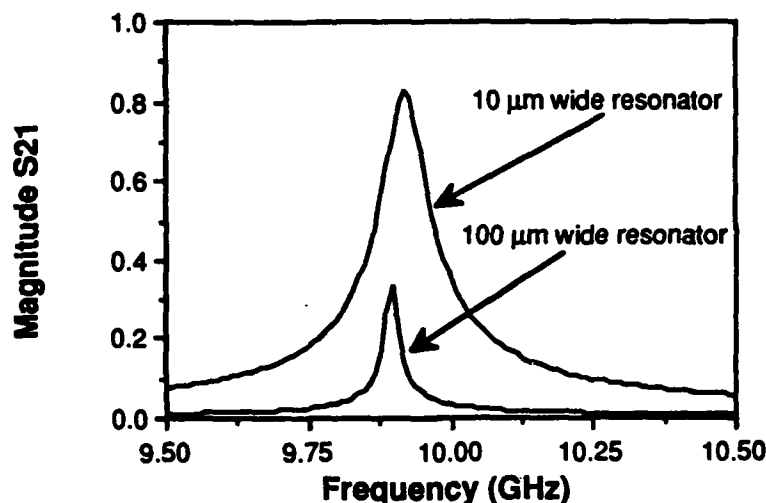


Figure 15. Frequency Response of Dielectric Step Coupled Resonators

The coupling mechanism is not completely understood. Some of the coupling is due to the overlap of the TEM modes in the two substrate regions. However, there is an additional coupling mechanism between the magnetic fields propagating in the superconductors themselves. Pond [32] has done some preliminary work to investigate this effect.

Due to the unknown nature of the coupling, the effective change in resonator length must be assumed to be a function of frequency. As discussed before, this can be corrected by using a full wavelength resonator and a half wavelength resonator. The resonant frequency will be almost the same and the line length difference will be large compared to the change in effective

line length due to the coupling. Three resonators were designed to resonate near 10 GHz using our model for propagation constant and simulated using Sonnet software. The width of all three were kept constant at 100  $\mu\text{m}$ , and the dielectric thickness was set to 0.1  $\mu\text{m}$ . The lengths were 0.55 cm, 0.57 cm, and 1.1 cm. The simulator predicted resonant frequencies of 10.23 GHz, 9.9 GHz, and 10.26 GHz. Using equation 3.1 with  $n_1=n_2=1$ , simulations on the 0.55 cm and 0.57 cm resonators compute an effective dielectric constant of 5.97. The 0.55 cm and 1.1 cm resonators with  $n_1=1$  and  $n_2=2$  yield an effective dielectric constant of 7.11 which is much closer to the value of 7.2 predicted by our model.

### 3.3.2 Impedance Matching Network

In order to measure the stepped dielectric resonator, a matching circuit is necessary. This matching network will create an interface between the low impedance resonator and a 50-ohm measurement system. The circuit designed is a tapered transmission line with a continuous impedance profile. At the input and output of the transformer are the 50-ohm measurement system and the 4.5-ohm resonator, respectively. In order to couple to the resonator, the low impedance end of the transformer should be MS. Since the thin film networks to be fabricated have no substrate via holes, MS will not be suitable for the high impedance end of the transformer. Instead, the high impedance end of the line will be implemented with CPW. This will allow an interface to 50-ohm SMA launchers. Thus, in addition to transforming from 50 ohms to a few ohms, the matching circuit must also physically change from CPW to MS.

#### 3.3.2.1 Physical Transformation

A method to physically change from a high impedance CPW to a low impedance MS has been demonstrated [33]. This method is compatible with the resonator circuits to be fabricated. Figure 2 shows a cross-sectional view of CPW. Figure 1 shows a cross-sectional view of MS. To make these two sections physically compatible, the center metal of the CPW is placed above the dielectric layer (see figure 16, which corresponds to section B as shown in figure 14(a)). As long as the horizontal dimensions are much larger than the vertical dimensions, the CPW models will still accurately describe this structure. Thus,  $S$ , the top plate width, and  $W$ , the gap, must be much larger than  $d$ , the dielectric thickness, and  $t$ , the metal thickness. The characteristic impedance of the CPW can be varied by changing  $S$  and  $W$ .

To allow more flexibility in the impedance values of the MS, and to smoothly transition to the CPW section of the transformer, a gap is introduced in the ground plane, as depicted in figure 17 (note that this drawing corresponds to section A of figure 14(a)). Comparing figures 16 and 17, it is seen that the top plate, dielectric layer, and ground plane are all consistent throughout the taper.

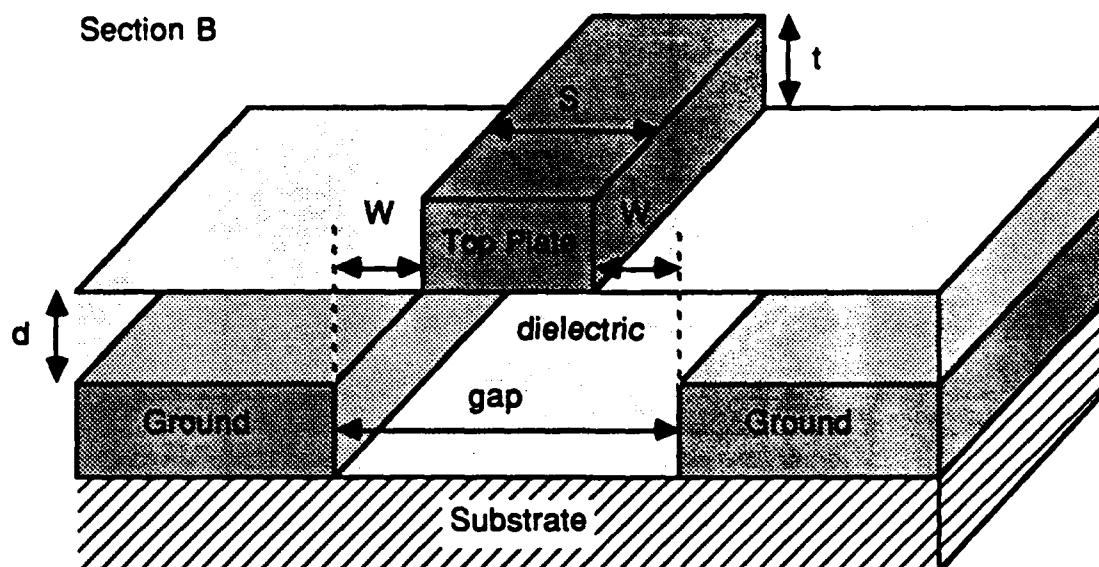


Figure 16. Modified Coplanar Waveguide

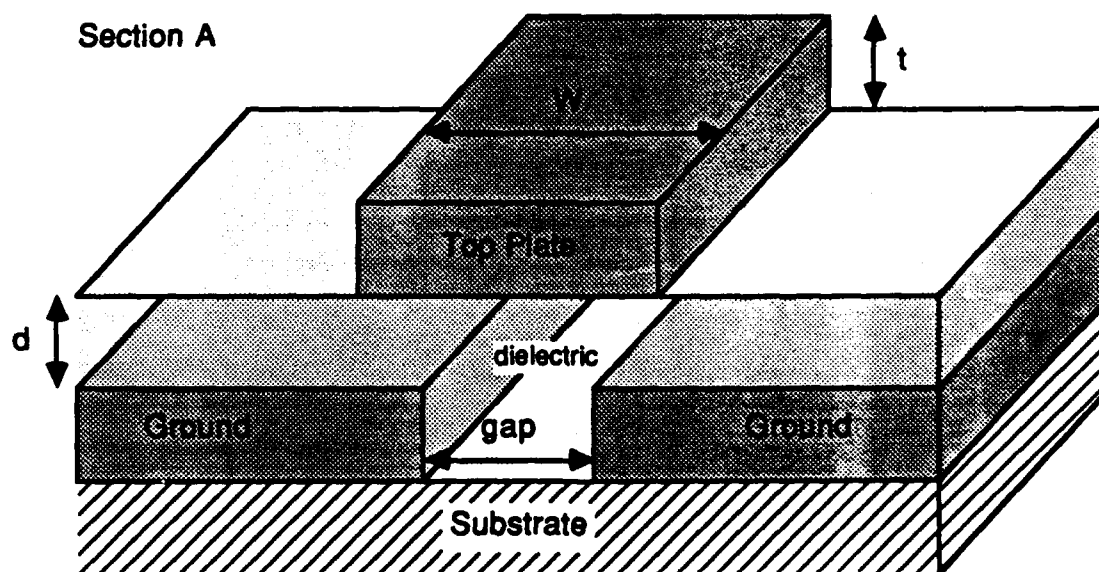


Figure 17. Microstrip with Gap in Ground Plane

The transformer will have a CPW high impedance region and a MS low impedance region. The CPW region occurs when the gap is larger than the top plate width. The MS region occurs when the gap is smaller than the plate width. In addition, there will also be a transition region, where the top plate and gap widths are close to the same value, where neither the CPW or MS models are valid.

### 3.3.2.2 Electrical Transformation

To change the impedance of the CPW and MS, the top plate and gap widths are varied to give a smooth impedance transformer. Four impedance profiles are considered, a linear, an exponential, a Dolph-Chebyshev, and a sinusoidal. These are all characterized by the impedance along the taper as a function of position. For the linear taper,

$$Z(x) = \frac{Z_2 - Z_1}{L}x + Z_1 \quad (50)$$

for the exponential taper, [34]

$$Z(x) = Z_1 \exp \frac{x}{L} \ln \frac{Z_2}{Z_1} \quad (51)$$

for the Chebyshev taper, [33]

$$Z(x) = Z_1 \exp \left\{ \frac{1}{2} \ln \frac{Z_2}{Z_1} \left[ \sin \left( \pi \left( \frac{x}{L} - \frac{1}{2} \right) \right) + 1 \right] \right\} \quad (52)$$

and for the sinusoidal taper,

$$Z(x) = \frac{Z_1 - Z_2}{2} \cos \left( \pi \frac{x}{L} \right) + \frac{Z_1 + Z_2}{2} \quad (53)$$

where  $L$  is the length of the taper,  $x$  is the position along the taper,  $Z_1$  is the impedance at  $x=0$  (the input impedance),  $Z_2$  is the impedance at  $x=L$  (the output impedance), and  $Z(x)$  is the impedance at the point  $x$ .

Figure 18 is a plot of impedance versus position ( $x$ ) along the taper for all four profiles. The length used is 10,000  $\mu\text{m}$ ,  $Z_1$  is fifty ohms, and  $Z_2$  is 4.5 ohms. Note that once either the position or impedance is specified, the other parameter is uniquely determined.

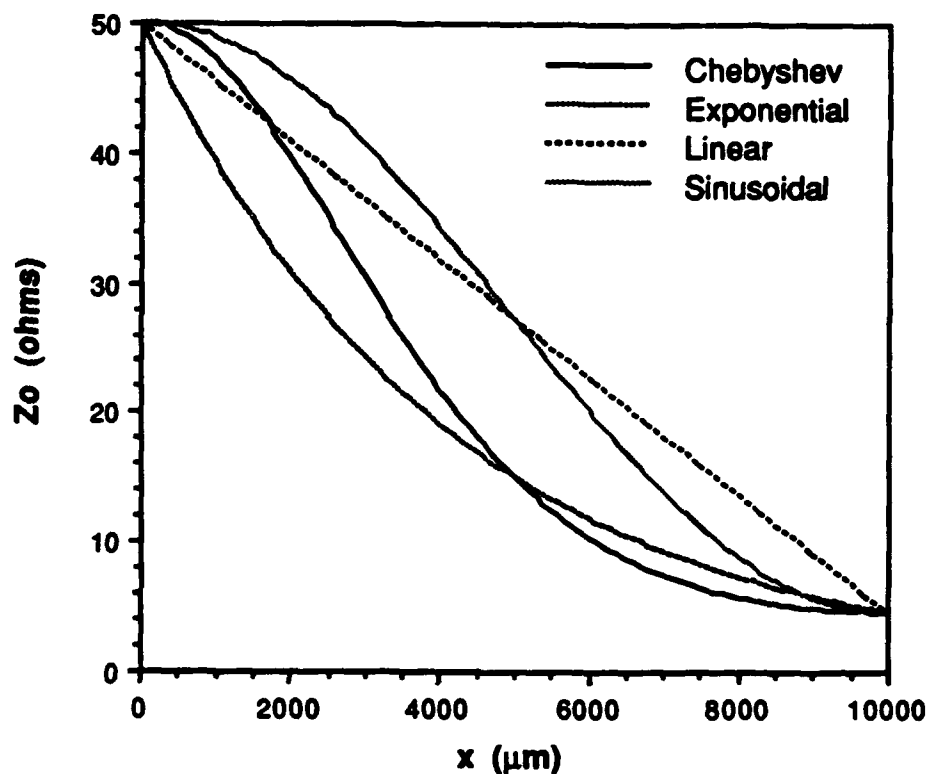


Figure 18. Plots of Impedance Versus Position for the Four Taper Profiles.

### 3.3.2.3 Initial Analysis

Except at very low frequencies, the transmission line taper acts like a high-pass filter with a cut-off frequency of [33]

$$f_c = \frac{cv_r}{2L} \quad (54)$$

where  $c$  is the speed of light in a vacuum and  $v_r$  is the relative velocity in the transmission line. For example, a relative phase velocity of 0.50 and a taper length of 10 mm gives a cut-off frequency of 7.5 GHz. This length of 10 mm is suitable for use with the resonator, which is

designed for 10 GHz and above. Furthermore, a 10-mm taper is a reasonable length for a superconducting test circuit.

To initially compare the four profiles, a microwave CAD program (Super-Compact) was used to simulate the tapers. This was accomplished by splitting each taper into a number of linear tapers, an element available in the simulator. This element has an output impedance, an input impedance, a length, and a phase velocity. If enough linear components are used, the Chebyshev, exponential and sinusoidal transformers can be accurately modeled.

A FORTRAN program was written to automatically create Super-Compact netlists for the four types of transformers. Inputs to this routine are the length of the transformer, the number of linear tapers to use, the input and output impedances of the transformer, and the phase velocity. The output from the program is a circuit file formatted for use with the microwave CAD program. The length of each linear taper is the total length divided by the number of tapers. The input and output impedances are calculated from the corresponding position along the transformer.

As a preliminary demonstration, a transformer circuit for each impedance profile is simulated. The transformers analyzed are ten millimeter tapers, each split into 100 linear tapers, with an input impedance of 50 ohms and an output impedance of 4.5 ohms. A phase velocity of fifty percent is assumed. The circuit simulated consists of the 50- to 4.5-ohm transformer, a delay line, and a 4.5- to-50-ohm transformer. The delay line is a 4.5-ohm, 10-mm transmission line with a phase velocity of 0.50. This circuit is similar to a structure that will actually be fabricated to test the transformer, *i.e.*, a taper to transform to a resistance below ten ohms, a low impedance superconducting transmission line, and another taper to transform back to fifty ohms. Figure 19 shows the insertion loss of all four transformers.



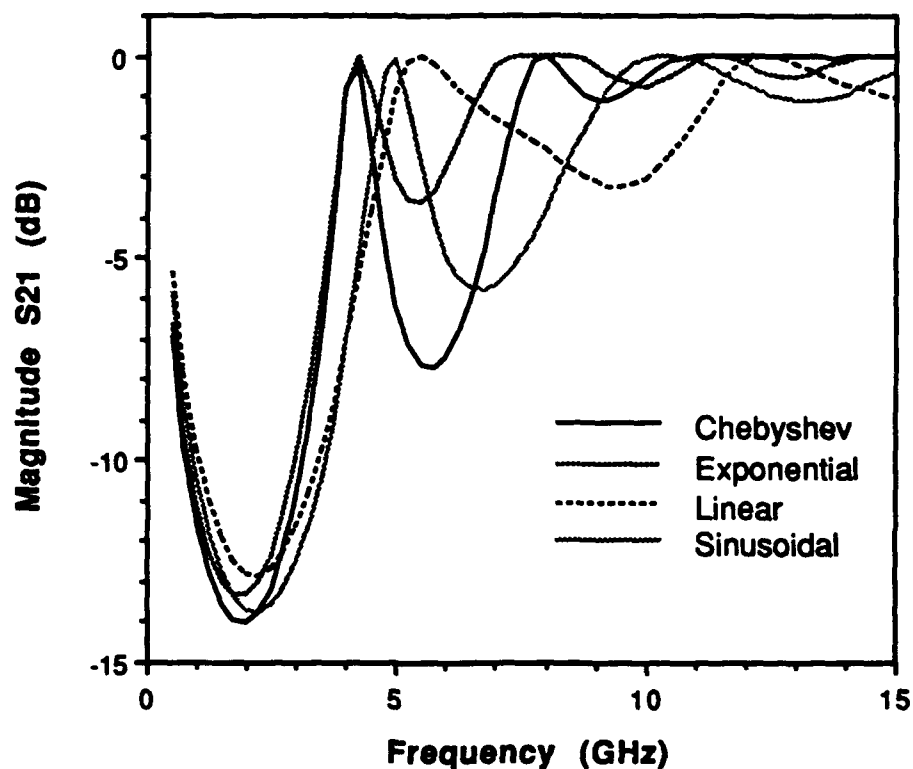


Figure 19. Responses of Four Transformers Using 0.50 Phase Velocity

Figure 19 shows that the linear taper has the greatest insertion loss in the frequency range of interest. In the 10-GHz region, the Chebyshev, exponential and sinusoidal responses are similar. The Chebyshev taper has the flattest passband (*i.e.*, above 10 GHz) response. Another important parameter is the reflection coefficient; the magnitude of  $S_{11}$  should be as small as possible.  $S_{11}$  is shown in figure 20. The linear taper has the worst performance; it is difficult to distinguish among the other three transformers.

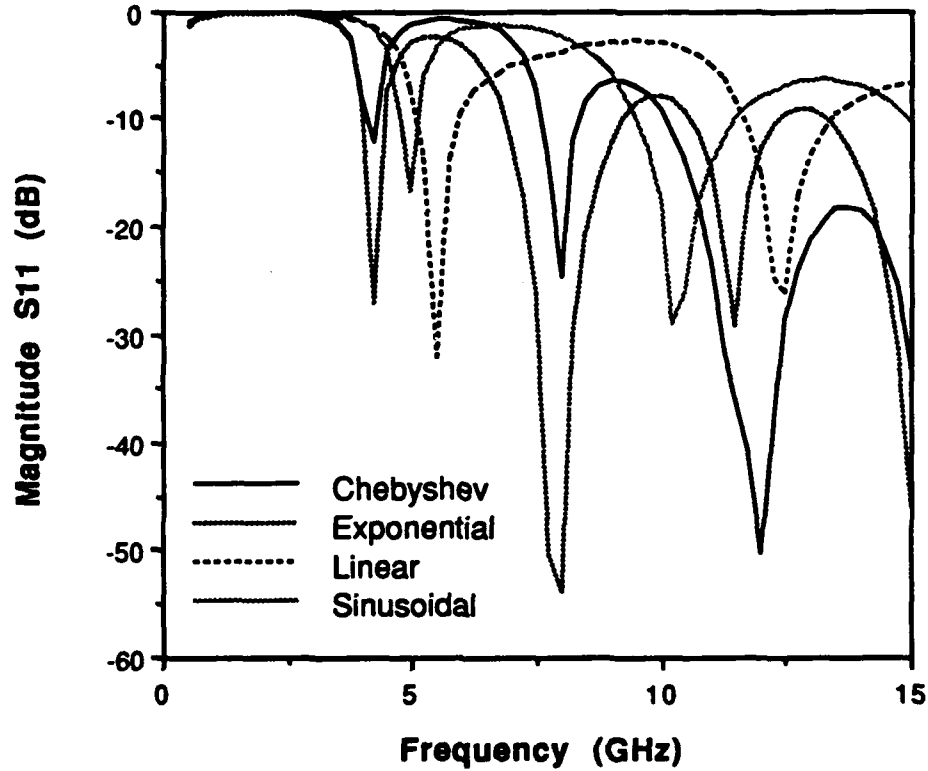


Figure 20. Reflection Coefficient of Four Transformers Using 0.50 Phase Velocity.

#### 3.3.2.4 Transmission Line Parameters

To physically realize the desired impedance profile, the top plate and gap widths are varied. In the CPW region, the characteristic impedance of the line is given by [19]

$$Z_o = \frac{30\pi}{\sqrt{\epsilon_{re}}} \frac{1}{G_1} \quad (55)$$

$\epsilon_{re}$  is the effective dielectric constant of the line.  $G_1$  is the complete elliptic integral of the first kind, approximated by [19]

$$G_1 = \pi \left\{ \ln \left[ 2 \frac{1 + \sqrt{k'}}{1 - \sqrt{k'}} \right] \right\}^{-1} \quad \text{for } 0 \leq k < \frac{1}{\sqrt{2}} \quad (56)$$

$$G_1 = \pi^{-1} \ln \left[ 2 \frac{1 + \sqrt{k'}}{1 - \sqrt{k'}} \right] \quad \text{for } \frac{1}{\sqrt{2}} \leq k \leq 1 \quad (57)$$

where

$$k = \frac{S}{S + 2W} \quad \text{and} \quad k' = \sqrt{1 - k^2} \quad (58)$$

The quasistatic value of the effective dielectric constant of the line is given by [19]:

$$\epsilon_{reo} = \frac{\epsilon_r + 1}{2} \left[ \tanh \left\{ 1.785 \log \frac{h}{W} + 1.75 \right\} + \frac{kW}{h} r \right] \quad (59)$$

and

$$r = \{0.04 - 0.7k + 0.01(1.0 - 0.1\epsilon_r)(0.25 + k)\} \quad (60)$$

where  $\epsilon_r$  is the relative dielectric constant of the substrate,  $h$  is the substrate height and  $W$  is the spacing between the lines (see figure 16). The following dispersion correction relates  $\epsilon_{re}$  as a function of frequency to  $\epsilon_{reo}$  [21]:

$$\sqrt{\epsilon_{re}(f)} = \sqrt{\epsilon_{reo}} + \frac{\sqrt{\epsilon_r} - \sqrt{\epsilon_{reo}}}{1 + aF^{-b}} \quad (61)$$

where

$$F = \frac{f}{f_{TE}} \quad \text{and} \quad f_{TE} = \frac{c}{4h\sqrt{\epsilon_r - 1}} \quad (62)$$

and [35]

$$b = 1.8 \quad (63)$$

$$\log(a) = u \log(S/W) + v \quad (64)$$

$$u = 0.54 - 0.64q + 0.015q^2 \quad (65)$$

$$v = 0.43 - 0.86q + 0.540q^2 \quad (66)$$

$$q = \log(S/h) \quad (67)$$

$S$  is the center line width (see figure 16).

The relative phase velocity in the line, as a percentage of the speed of light, is given by [21]:

$$v_p = \frac{1}{\sqrt{\epsilon_n}} \quad (68)$$

The horizontal dimensions of the modified CPW must be an order of magnitude greater than the vertical dimensions. Thus,

$$S, W \geq 10d \text{ and } S, W \geq 10t \quad (69)$$

In the MS region the line can be modeled as a parallel-plate transmission line [33]. The characteristic impedance is given by:

$$Z_o = \frac{d}{W - G} \sqrt{\frac{\mu_o}{\epsilon_o \epsilon_r}} \sqrt{\frac{2\lambda_L + d}{d}} \quad (70)$$

where  $d$  is the dielectric thickness,  $W$  is the top plate width,  $G$  is the gap width,  $\epsilon_r$  is the relative dielectric constant of the dielectric layer, and  $\lambda_L$  is the London penetration depth of the superconducting metals. This equation is valid for

$$W - G \geq 20d \quad (71)$$

The phase velocity is given by:

$$v_p = \sqrt{\frac{1}{\mu_o \epsilon_o \epsilon_r}} \sqrt{\frac{d}{2\lambda_L + d}} \quad (72)$$

Equation 33 can be solved to give the effective dielectric constant in the MS region:

$$\epsilon_n = \frac{1}{v_p^2} \quad (73)$$

In the CPW region, propagation occurs largely in the substrate. Thus, the equations for  $Z_o$  and  $\epsilon_r$  are functions of the metal widths and substrate parameters, but not a function of the thickness or  $\epsilon_r$  of the dielectric layer. Conversely, propagation in the MS occurs between the metal plates, in the dielectric layer. Here,  $Z_o$  and  $\epsilon_r$  are functions of the metal widths and dielectric layer parameters, but not a function of the substrate height or substrate dielectric constant.

For MS, since the wave is traveling in the dielectric layer, and the dielectric thickness is of the same order as the metal thicknesses, the penetration depth of the wave into the superconducting metals is important. Hence the London penetration term ( $\lambda_L$ ) occurs in the MS equations. For CPW however, propagation is in the substrate. Since the substrate height is much larger than the metal thickness, penetration effects are ignored.

### 3.3.2.5 Determining the Widths of the Top Plate and Gap

With the CPW and MS equations, the top plate and gap widths can be determined to give any desired impedance. The top plate width must be 550  $\mu\text{m}$  at the CPW input to interface to SMA launchers. To be compatible with the resonator to be tested, at the end of the MS region, the top plate width must be ten microns wide and the gap width must narrow down to zero. However, in the transition region, neither the CPW nor MS models are valid. The exact characteristics of this region are cannot be exactly determined. Therefore, the length of the transition region should be minimized. This is done by making the CPW and MS regions as long as possible.

The length of the CPW region is maximized by minimizing the impedance at the start of the transition. The end of the CPW region occurs when  $W$  (the spacing between top metal and ground plane) is at its minimum value (equation 69). The CPW equations show that for a fixed  $W$ , the characteristic impedance decreases as  $S$  (the top plate width) increases. As a result, the top metal width is kept constant through the CPW region. Decreasing the top metal width will increase the transition region length. The top plate width should not increase in the CPW region since this metal must smoothly narrow down to a ten micron wide line. Large changes in metal widths over short distances could add unmodeled and unwanted discontinuities.

In the MS region, the impedance is inversely proportional to the top metal width minus the gap width (equation 70). The length of the MS region is maximized by maximizing the impedance at the transition point. This occurs by making  $W-G$  as small as possible. This is limited by the validity of equation 70, shown by equation 72. Once the minimum value of  $W-G$  for MS is given, the maximum MS impedance and therefore the position of the end of the transition region is determined. Changing  $W$  cannot move this point. For this reason,  $W$  is also held constant throughout the MS region. Thus, the top plate width is a constant 550  $\mu\text{m}$  in the CPW region, and a constant 10  $\mu\text{m}$  in the MS region. Note that this also has the advantage of simplifying the layout of the top metal.

Since the impedance at each point along the transformer is known, the gap width can be determined once the top plate width has been specified. For the MS region, equation 70 can be solved for the gap width:

$$G = W - \frac{d}{Z_o} \sqrt{\frac{\mu_o}{\epsilon_o \epsilon_r}} \sqrt{\frac{2\lambda_L + d}{d}} \quad (74)$$

For the CPW region, no simple expression exists for the gap width based on the top plate width and the characteristic impedance. Therefore, an iterative method must be used to calculate the gap width for this region.

In the transition region, the top plate and gap widths should smoothly change from their values at the end of the coplanar region to their values at the beginning of the MS region. This was accomplished by approximating these shapes as cubic polynomials. In addition to the top plate and gap widths, the derivatives of these shapes with respect to  $x$  (the position along the taper) at the interfaces will be kept consistent. This gives four equations in four unknowns:

$$A(x_1)^3 + B(x_1)^2 + Cx_1 + D = y_1 \quad (75)$$

$$3A(x_1)^2 + 2Bx_1 + C = y_1' \quad (76)$$

$$A(x_2)^3 + B(x_2)^2 + Cx_2 + D = y_2 \quad (77)$$

$$3A(x_2)^2 + 2Bx_2 + C = y_2' \quad (78)$$

where, using the top plate width as an example:

$x_1$  is the value of  $x$  at the end of the CPW region (the start of the transition);

$x_2$  is the value of  $x$  at the start of the MS region (the end of the transition);

$y_1$  is the width of the top plate at  $x=x_1$ ;

$y_1'$  is the derivative of the top plate at  $x=x_1$ ;

$y_2$  is the width of the top plate at  $x=x_2$ ;

$y_2'$  is the derivative of the top plate at  $x=x_2$ .

This system of equations is established and solved for both the top plate width and the gap width, allowing these structures to be calculated in the transition region.

A FORTRAN program has been written to automatically generate data to draw the masks and files to simulate the taper. This routine is completely general, that is, all of the parameters of the metals, dielectric, substrate, and taper can be entered. The routine accepts the taper length; the desired input and output impedance; the number of tapers to break the transformer into; the height and relative dielectric constant of the substrate; the thickness and relative dielectric constant of the dielectric layer; the penetration depth of the superconducting metal; the frequency (used for dispersion correction); the desired width of the top plate in the CPW region; the desired width of the top plate in the MS region; and the limits on the validity of the characteristic impedance equations.

The routine assumes only that the top plate width is constant in the CPW and MS regions. For all four impedance profiles, the routine calculates the exact locations where the CPW and MS models are no longer valid, that is, the exact location of the transition region is found. The gap width needed to give the necessary impedance is found for the CPW and MS regions. Information on the top plate and gap is used to fit the cubic polynomials in the transition region. A data file showing the width of the top plate and gap is created. This file could be used to digitize the masks.

### 3.3.2.6 Improved Analysis

The FORTRAN routine also creates Super-Compact netlist files for each transformer. The program calculates the exact phase velocity at the midpoint of each linear taper. This gives a much more accurate prediction of the performance than the preliminary analyses shown in section 3.3.2.3. Since the models cannot be used to predict the phase velocity in the transition region, this parameter is also fit to a cubic.

An example is shown in tables 2 and 3 to demonstrate the use of the routine. For the MS region, a ten micron wide top metal gives a minimum  $Z_0$  of 5.14 ohms. This impedance value is entered as the desired output impedance. This minimum value of  $Z_0$  occurs when the gap width is zero. The output data is summarized in table 3-3. Note that the Chebyshev and sinusoidal tapers have the added advantage of having the shortest transition regions, where the impedance and relative phase velocity cannot be modeled exactly. The circuit simulated consists of the 50-to 5.14-ohm transformer, a delay line, and a 5.14- to 50-ohm transformer. The delay line is a 5.14-ohm, 10-mm transmission line with a phase velocity of 0.367. The responses of the four tapers are shown in figures 21 and 22.

Table 2. Inputs to Taper Routine

Taper length	10 mm
Impedance at input	50 ohms
Impedance at output	5.14 ohms
Number of tapers	100
Substrate height	100 $\mu\text{m}$
Substrate $\epsilon_r$	4
Dielectric thickness	0.2 $\mu\text{m}$
Dielectric $\epsilon_r$	4
Penetration depth (niobium)	0.086 $\mu\text{m}$
Frequency	10 GHz
CPW limit	$W \geq 10d$
MS limit	$W - G \geq 20d$

Table 3. Summary of Output from Taper Routine

	Top Metal Width	Gap Width	Phase Velocity
Start of Taper	550.0 $\mu\text{m}$	622.2 $\mu\text{m}$	0.705
Start of Transition	550.0 $\mu\text{m}$	554.0 $\mu\text{m}$	0.637
End of Transition	10.0 $\mu\text{m}$	6.0 $\mu\text{m}$	0.367
End of Taper	10.0 $\mu\text{m}$	0.0 $\mu\text{m}$	0.367

	Start of Transition	End of Transition	Length of Transition
Chebyshev Taper	$x = 3496.3 \mu\text{m}$	$x = 5623.4 \mu\text{m}$	2127.1 $\mu\text{m}$
Exponential Taper	$x = 2724.8 \mu\text{m}$	$x = 5973.0 \mu\text{m}$	3248.2 $\mu\text{m}$
Linear Taper	$x = 5149.7 \mu\text{m}$	$x = 8282.1 \mu\text{m}$	3132.4 $\mu\text{m}$
Sinusoidal Taper	$x = 5095.3 \mu\text{m}$	$x = 7279.3 \mu\text{m}$	2184.0 $\mu\text{m}$

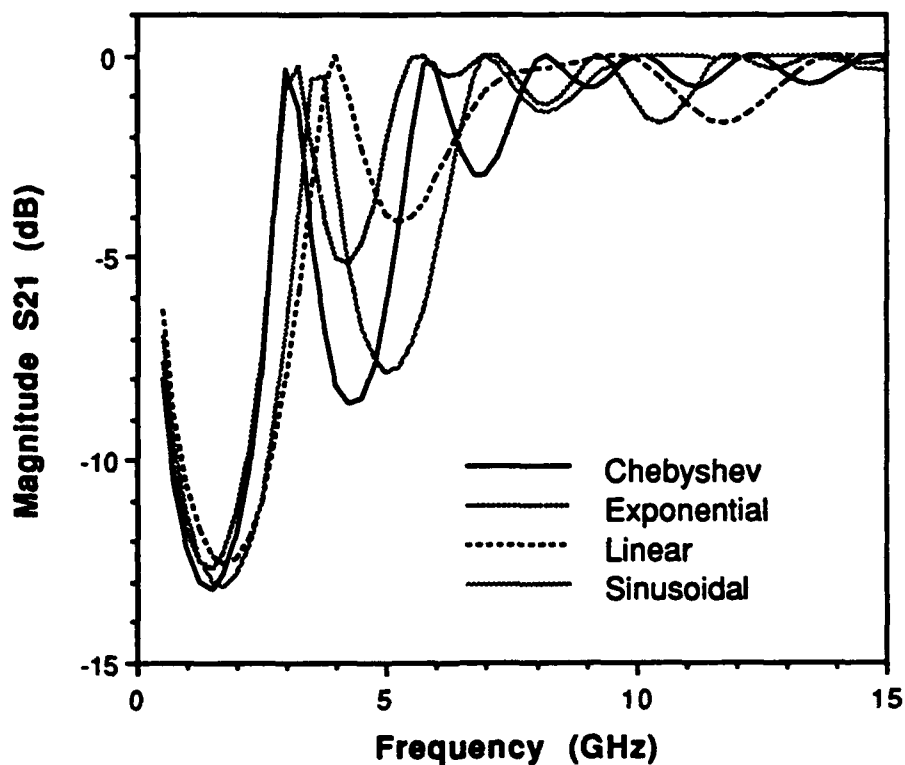


Figure 21. Transformer Responses Using Exact Calculation of Phase Velocity



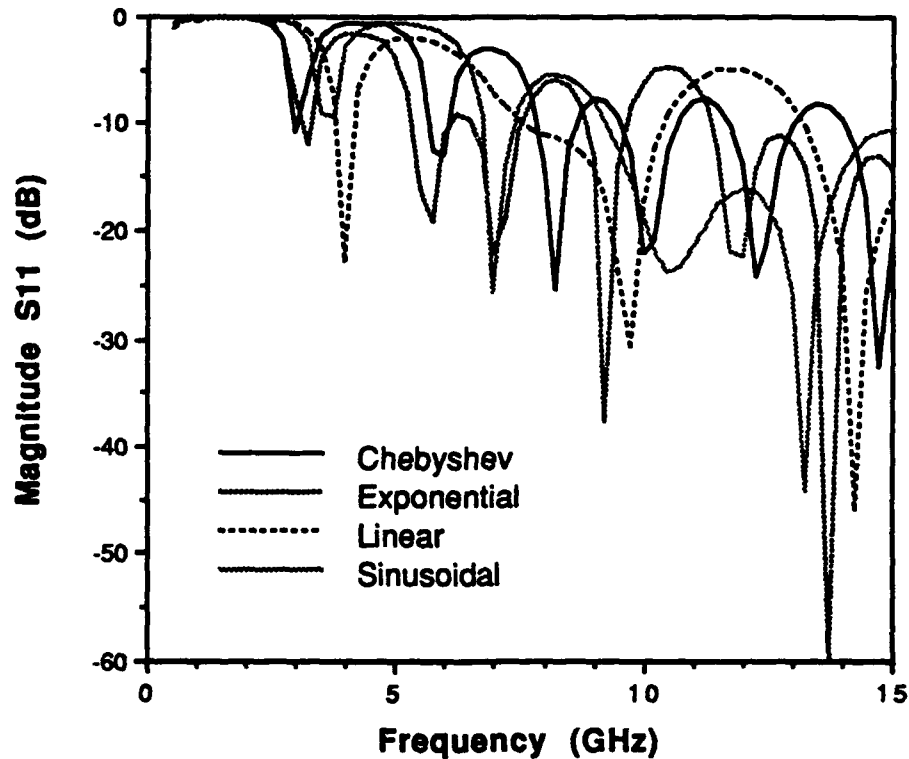


Figure 22. Transformer Responses Using Exact Calculation of Phase Velocity

The sinusoidal transformer is the best for this particular example since it has the flattest passband response (figure 21), although the Chebyshev taper would also be a reasonable choice. The plot of  $S_{11}$  (figure 22) is inconclusive since all four tapers exhibit similar performance. The responses have changed significantly from figure 19 due to the inclusion of the exact calculation of the phase velocity. The mask data from the sinusoidal transformer is plotted. Figure 23 shows a plot of the top plate and gap widths along the taper. Note that both structures are continuous and smooth.

### 3.3.3 Substrate Resonances

The transformer described is based on work done by McGinnis and Beyer [33]. Assuming a fixed phase velocity, they successfully designed and fabricated a 50- to 2-ohm Chebyshev transformer. However, they observed dropouts in the response of the transformer fabricated

which they attributed to substrate resonances. These dropouts occurred near 4.5 GHz and 8 GHz and caused almost 10 dB more loss in the circuit than predicted. We investigated this phenomenon through research and simulations on dielectric resonators to insure that similar problems would not affect our experiment.

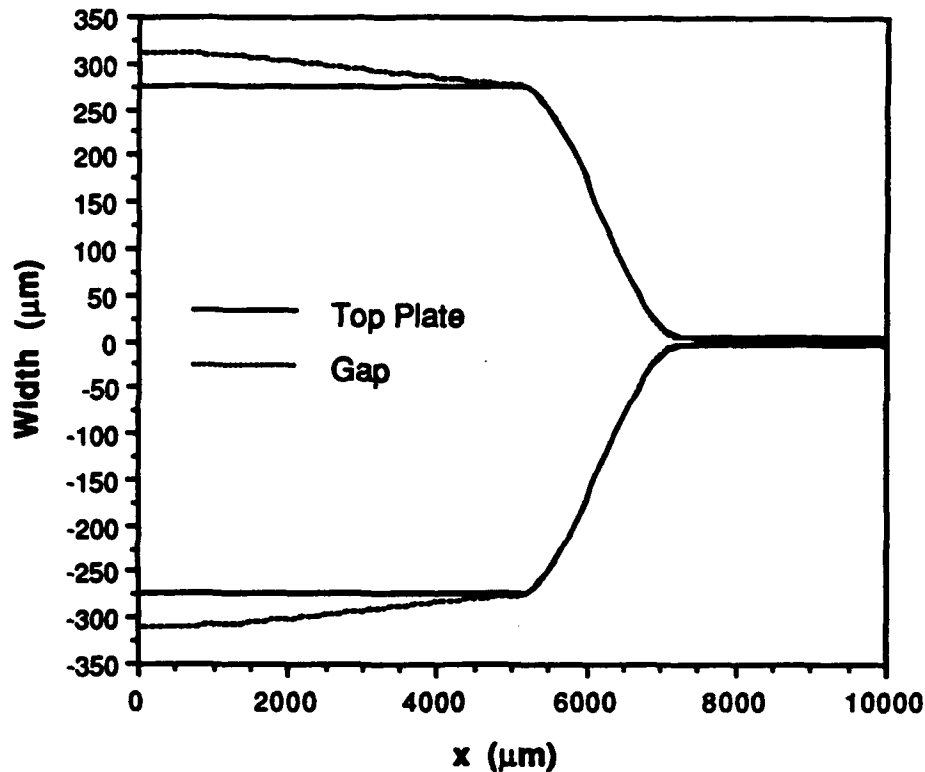


Figure 23. Plot of Top Plate and Gap for the Sinusoidal Transformer

The McGinnis and Beyer circuit is fabricated on a square substrate 25 mm on a side. This is shown in figure 24. The location of the input and output ports are shown. The height of the substrate is 400  $\mu\text{m}$ ; the dielectric constant of the substrate is 12.

The resonant frequency of a cylindrical dielectric resonator can be approximated by:[36]

$$f(\text{GHz}) = \frac{1}{\sqrt{\epsilon_r}} \left( \frac{34}{L(\text{mm})} + \frac{117.3}{r(\text{mm})} \right) \quad (79)$$

where  $r$  is the radius,  $L$  is the length,  $\epsilon_r$  is the dielectric constant. Instead of a cylindrical resonator, the case here is a dielectric slab with a height  $400\text{ }\mu\text{m}$  and a width  $25\text{ mm}$ . However, the experiment will be fabricated on a  $100\text{-}\mu\text{m}$  substrate with a dielectric constant of 4. Since the resonant frequency is inversely proportional to the square root of  $\epsilon_r$ , reducing this by a factor of 3 will increase the frequency by a factor of 1.7. Furthermore, if  $L$  is large, the frequency becomes inversely proportional to  $r$ , and thus decreasing the substrate thickness by a factor of 4 will also move the resonances to a higher frequency.

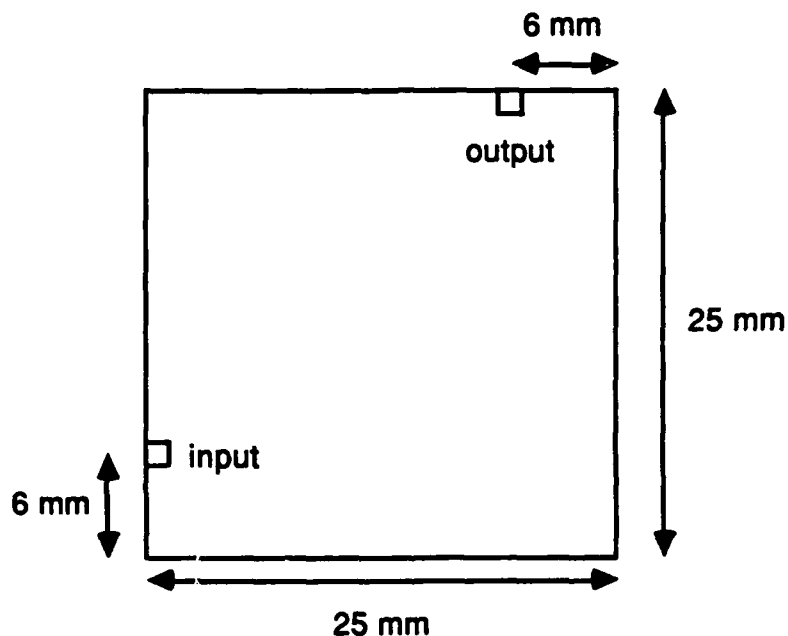


Figure 24. Substrate and Ports Used by McGinnis and Beyer

To show this numerically, Sonnet Software's EM simulator was used to simulate the throughput between isolated ports on dielectric slabs. The slab (except for thickness) and ports are constructed the same as the McGinnis circuit (see figure 3-14). Four simulations are performed:

$h = 400\text{ }\mu\text{m}$ ,  $\epsilon_r = 12$  (the situation in the McGinnis paper)

$h = 400\text{ }\mu\text{m}$ ,  $\epsilon_r = 4$

$h = 100\text{ }\mu\text{m}$ ,  $\epsilon_r = 12$

$h = 100\text{ }\mu\text{m}$ ,  $\epsilon_r = 4$  (the situation of the current experiment)

Figure 25 is a plot of the predicted responses. The  $h = 400 \mu\text{m}$ ,  $\epsilon_r = 12$  simulation shows several peaks in  $S_{21}$  near 10 GHz. Decreasing either parameter generally reduces  $S_{21}$ . Decreasing both parameters effectively reduces the signal between the ports to a minimal level, especially in the frequency range of concern (the 10 GHz region).

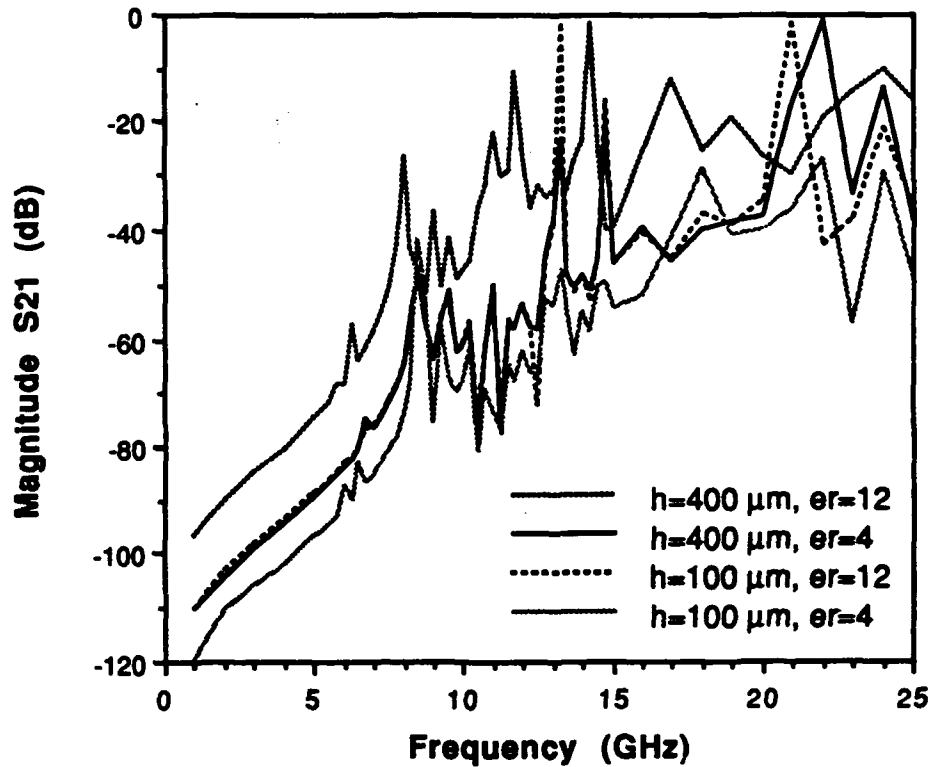


Figure 25. Isolated Ports on a 25-mm by 25-mm Dielectric Slab

EM simulations were also run on the substrate to be used for the resonator experiment. This substrate is 30 mm by 0.5 mm. To again illustrate the effects of reducing the substrate height and decreasing the dielectric constant, simulations are performed on a substrate with the following parameters:

$$h = 400 \mu\text{m}, \epsilon_r = 12$$

$$h = 400 \mu\text{m}, \epsilon_r = 4$$

$$h = 100 \mu\text{m}, \epsilon_r = 12$$

$$h = 100 \mu\text{m}, \epsilon_r = 4$$

Figure 26 shows  $S_{21}$  between isolated ports on a 30-mm by 0.5-mm substrate. The simulation shows that for the  $\epsilon_r = 4$ ,  $h = 100 \mu\text{m}$  case, the ports are well isolated.

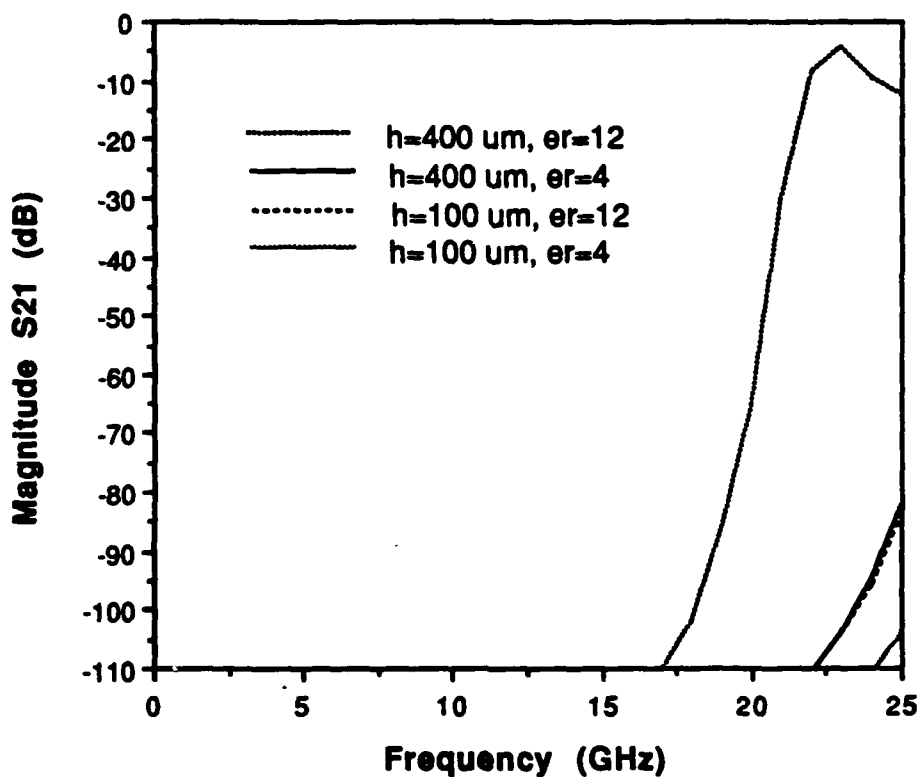


Figure 26. Isolated Ports on a 30-mm by 0.5-mm Dielectric Slab

### 3.3.4 Summary

The complete dielectric step coupled resonator with impedance matching transformer is illustrated in figure 27. There are three mask layers, the ground plane (red), the center conductor (blue) and the resonator (green). The placement of the three layers relative to each other is illustrated. Figure 28 depicts top and cross-sectional views of this same layout (as shown in figure 27).

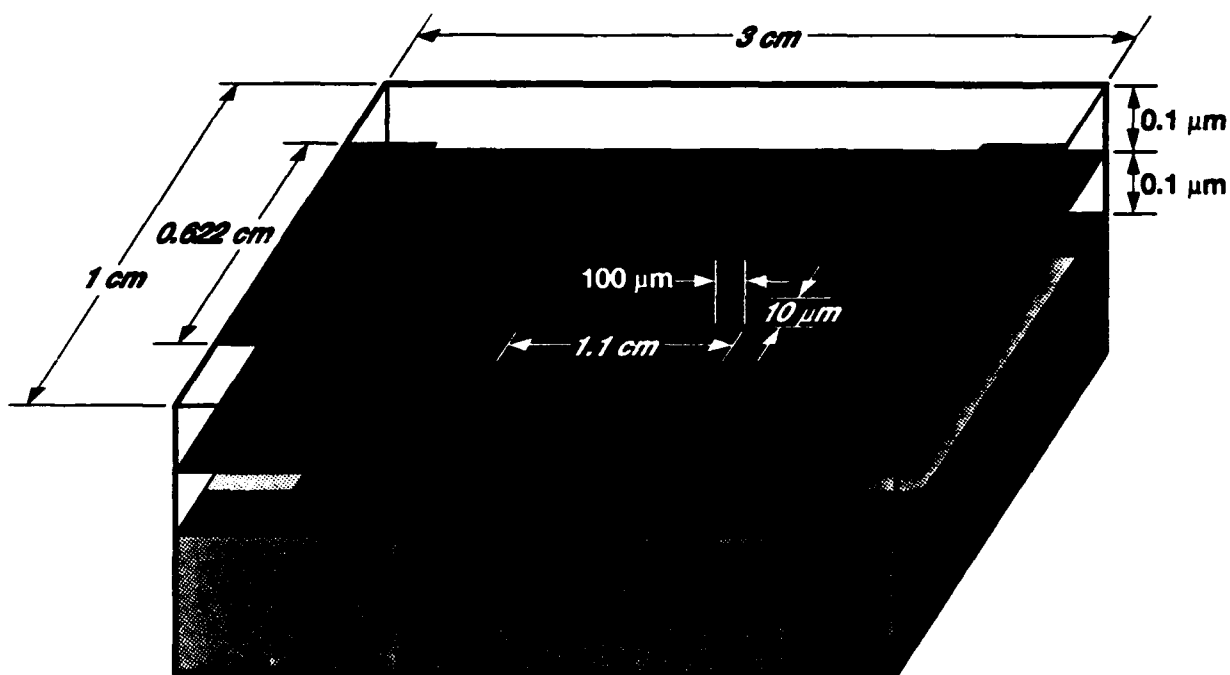


Figure 27. Complete Dielectric Step Coupled Resonator, Perspective View

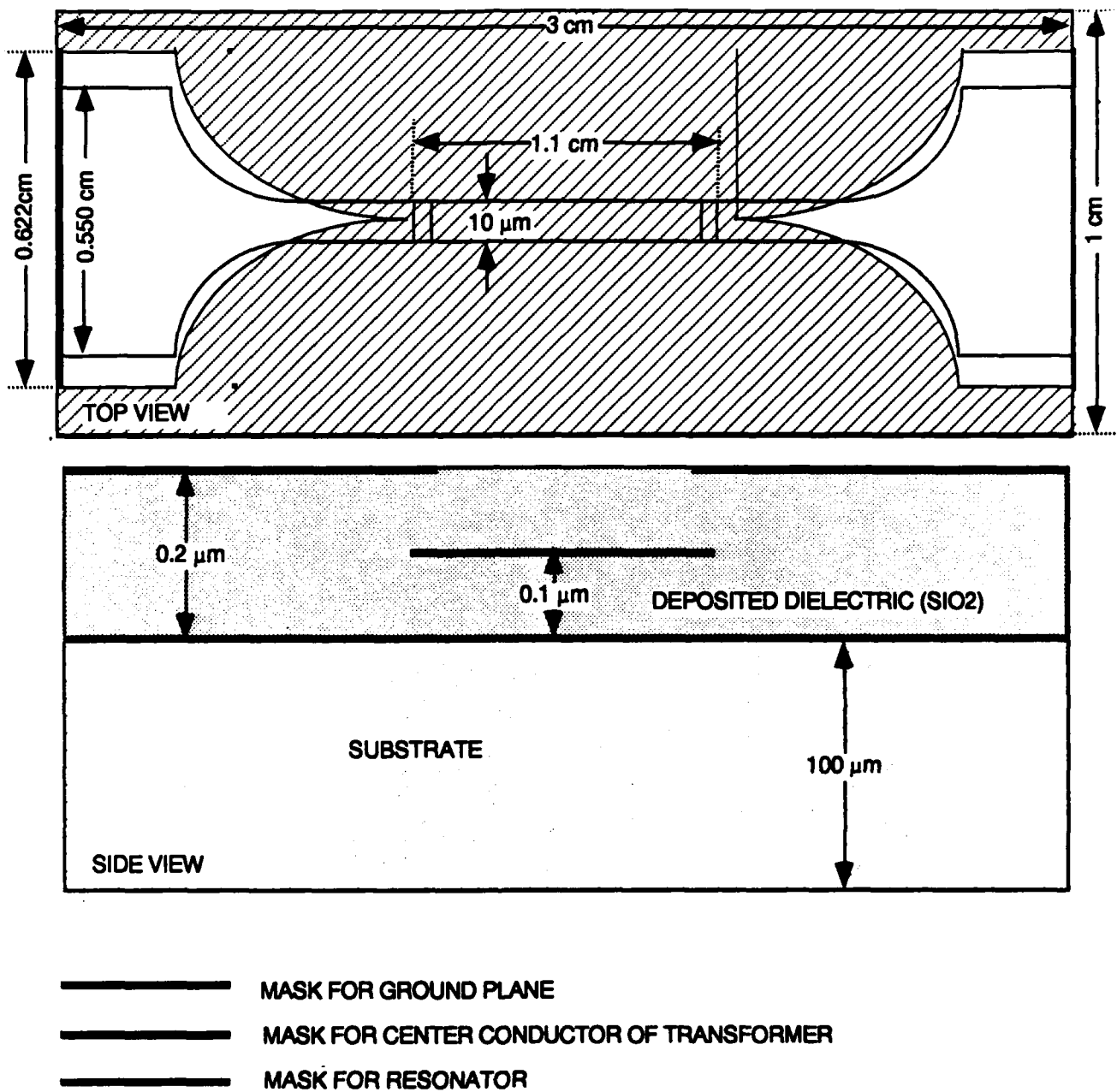


Figure 28. Complete Dielectric Step Coupled Resonator, Top and Cross-Sectional Views

## SECTION 4

### CONCLUSIONS/RECOMMENDATIONS

The accepted quasistatic planar waveguide models are not at issue when simulating superconducting transmission lines, but rather, the conventional model for conductor surface resistance and losses. Superconducting materials exhibit a strongly inductive surface *impedance* whose losses are proportional to the square of frequency, in contrast to the conventional surface resistance varying as the square root of frequency. For accurate modeling of superconducting transmission lines these effects must be accounted for. This can be conveniently accomplished through the use of a complex surface impedance  $Z_s$ , calculated from the superconductor complex conductivity, in the accepted MS and CPW equations. Unfortunately, commercially available CAD tools do not allow the conductivity or surface resistance of a material to be complex quantities.

It is necessary that accurate computer-aided design models be included in existing MMIC design software (for example, *Touchstone*, *SuperCompact* and SPICE) to effectively integrate superconducting materials into the realm of MMIC design. During this investigation we have developed models of superconducting transmission lines which can be interfaced with commercially available MMIC design software, either by embedding the models into the simulation software or by deriving equivalent circuit models. Equivalent circuit models could be substituted for the superconducting MS, allowing simulation of superconducting microwave circuits without requiring the modification of the simulation software code. Alternately, our superconducting transmission line model could be used to calculate scattering parameter data in a form suitable for input into the CAD simulator, treating the superconducting transmission line as a two-port device.

An experiment for verifying the superconducting transmission line models has been proposed. The experiment requires two resonators,  $1/2$  and  $1$  wavelength long. We have decided to perform the experiments at 10 GHz which is a compromise between small size circuits, and radiation losses. MS geometry has been chosen due to the ability to fabricate thin dielectric substrates. We have decided to use a  $0.1\text{ }\mu\text{m}$  dielectric layer for all measurements.

Two measurement circuits are proposed. The first is a  $100\text{ }\mu\text{m}$  wide, 0.5-ohm resonator coupled to its test ports by 50-ohm coaxial to MS launchers. The second circuit is a  $10\text{-}\mu\text{m}$  wide, 5-ohm MS coupled to the measurement system by a dielectric step and a 50 to 5-ohm transition section. The transition section ends in a 50-ohm CPW section. The dielectric step coupling has been simulated with Sonnet software's EM simulator. A mask large enough to set up both circuits will be a reasonable size. A foundry which can generate both circuits using niobium metalization and  $\text{SiO}_2$  dielectric should be used. These circuits will require  $0.01\text{-}\mu\text{m}$  accuracy in dielectric film thickness and  $2\text{-}\mu\text{m}$  accuracy in photolithography.



Many existing systems can be improved, and many new systems will become realizable with the use of superconducting microwave transmission lines. We have developed models for these transmission lines which are suitable for inclusion in commercial microwave circuit CAD software. We have also designed experiments which will allow us to verify the accuracy of these models.

## LIST OF REFERENCES

1. Withers, R. S. and R.W. Ralston, Aug. 1989, "Superconductive Analog Signal Processing Devices," *Proceedings of the IEEE*, Vol. 77, No. 8, p. 1247.
2. Pond, J. M., J.H. Claasen, and W.L. Carter, Dec. 1987, "Measurements and Modeling of Kinetic Inductance Microstrip Delay Lines," *IEEE Transactions on Microwave Theory and Techniques*, Vol. MTT-35, No. 12, pp. 1256-1262.
3. London, F., 1961, *Superfluids: Macroscopic Theory of Superconductivity*, Dover Publications, Inc., New York, Vol. 1.
4. Cooper, L. N., 15 Nov. 1956, "Bound Electron Pairs in a Degenerate Fermi Gas," *Physical Review*, Vol. 104, No. 4, pp. 1189-1190.
5. Bardeen, J., L. N. Cooper, and J. R. Schrieffer, 1 Dec. 1957, "Theory of Superconductivity," *Physical Review*, Vol. 108, No. 5, pp. 1175-1204.
6. Rose-Innes, A. C., and E. H. Rhoderick, 1978, *Introduction to Superconductivity*, Pergamon Press, New York.
7. Van Duzer, T., and C. W. Turner, 1981, *Principles of Superconductive Devices and Circuits*, Elsevier North Holland, Inc., New York.
8. Kautz, R. L., Jan. 1978, "Picosecond Pulses on Superconducting Striplines," *Journal of Applied Physics*, Vol. 49, No. 1, pp. 308-314.
9. Mattis, D. C., and J. Bardeen, 15 July 1958, "Theory of the Anomalous Skin Effect in Normal and Superconducting Metals," *Physical Review*, Vol. 111, No. 2, pp. 412-417.
10. Wolf, E. L., 1985, *Principles of Electron Tunneling Spectroscopy*, Oxford University Press, New York.
11. Thouless, D. J., 1 Mar. 1960, "Strong-Coupling Limit in the Theory of Superconductivity," *Physical Review*, Vol. 117, No. 5, pp. 1256-1260.
12. Sheahen, T. P., 9 Sept. 1966, "Rules for the Energy Gap and Critical Field of Superconductors," *Physical Review*, Vol. 149, No. 1, pp. 368-370.
13. Hartwig, W. H., and C. Passow, 1975, "RF Superconducting Devices," in *Applied Superconductivity*, V. L. Newhouse, ed., Academic Press, New York, Vol. II, pp. 541-639.

14. Turneure, J. P., and I. Weissman, Aug. 1968, "Microwave Surface Resistance of Superconducting Niobium," *Journal of Applied Physics*, Vol. 39, No. 9, pp. 4417-4427.
15. Gallagher, W. J., C.-C. Chi, I. N. Duling, III, D. Grischkowsky, N. J. Halas, M. B. Ketchen, and A. W. Kleinsasser, 9 Feb. 1987, "Subpicosecond Optoelectronic Study of Resistive and Superconductive Transmission Lines," *Applied Physics Letters*, Vol. 50, No. 6, pp. 350-352.
16. Dykaar, D. R., R. Sobolewski, J. M. Chwalek, J. F. Whitaker, T. Y. Hsiang, G. A. Mourou, D. K. Lathrop, S. E. Russek, and R. A. Buhrman, 25 Apr. 1988, "High-Frequency Characterization of Thin-film Y-Ba-Cu Oxide Superconducting Transmission Lines," *Applied Physics Letters*, Vol. 52, No. 17, pp. 1444-1446.
17. Nuss, M. C., P. M. Mankiewich, R. E. Howard, B. L. Straughn, T. E. Harvey, C. D. Brandle, G. W. Berkstresser, K. W. Goossen, and P. R. Smith, 29 May 1989, "Propagation of Terahertz Bandwidth Electrical Pulses on  $\text{YBa}_2\text{Cu}_3\text{O}_{7.8}$  Transmission Lines on Lanthanum Alluminate," *Applied Physics Letters*, Vol. 54, No. 22, pp. 2265-2267.
18. Matick, R. E., 1969, *Transmission Lines for Digital and Communication Networks*, McGraw-Hill Book Co., New York.
19. Gupta, K. C., R. Garg, and I. J. Bahl, 1979, *Microstrip Lines and Slotlines*, Artech House Inc., Norwood, MA.
20. Hsiang, T. Y., J. F. Whitaker, R. Sobolewski, D. R. Dykaar, and G. A. Mourou, 9 Nov. 1987, "Propagation Characteristics of Picosecond Electrical Transients on Coplanar Striplines," *Applied Physics Letters*, Vol. 51, No. 19, pp. 1551-1553.
21. Whitaker, J. F., R. Sobolewski, D. R. Dykaar, T. Y. Hsiang, and G. A. Mourou, Feb. 1988, "Propagation Model for Ultrafast Signals on Superconducting Dispersive Striplines," *IEEE Transactions on Microwave Theory and Techniques*, Vol. MTT-36, No. 2, pp. 277-285.
22. Ekholm, E. B., and S. W. McKnight, Apr. 1990, "Attenuation and Dispersion for High- $T_c$  Superconducting Microstrip Lines," *IEEE Transactions on Microwave Theory and Techniques*, Vol. MTT-38, No. 4, pp. 387-395.
23. Yamashita, E., K. Atsuki, and T. Ueda, Dec. 1979, "An Approximate Dispersion Formula of Microstrip Lines for Computer-Aided Design of Microwave Integrated Circuits," *IEEE Transactions on Microwave Theory and Techniques*, Vol. MTT-27, No. 12, pp. 1036-1038.

24. Ramo, S., J. R. Whinnery, and T. Van Duzer, 1984, *Fields and Wave in Communication Electronics*, Second Edition, Wiley, New York.
25. Pucel, R. A., D. J. Masse, and C. P. Hartwig, June 1968, "Losses in Microstrip," *IEEE Transactions on Microwave Theory and Techniques*, Vol. MTT-16, No. 6, pp. 342-350.
26. Drissi, M., V. Fouad Hanna, and J. Citerne, 1989, "Analysis of Radiating End Effects of Symmetric and Asymmetric Coplanar Waveguide Using Integral Equations Technique," *IEEE MTT-S Digest*, pp. 791-792.
27. Gopinath, A., 1982, "Losses in Coplanar Waveguides," *IEEE Transactions on Microwave Theory and Techniques*, Vol. 30, pp. 1101-1104.
28. Belohoubek, E., and E. Delinger, June 1975, "Loss Considerations for Microstrip Resonators," *IEEE Transactions on Microwave Theory and Techniques*, pp. 522-526.
29. Kajfez, D., and E.J. Hwan, 1984, "Q-Factor Measurement with Network Analyzer," *IEEE Transactions on Microwave Theory and Techniques*, Vol.32, pp. 666-670.
30. Ginzton, E. L., 1957, *Microwave Measurements*, New York, NY, McGraw-Hill.
31. McAvoy, B. R., G.R. Wagner, J.D. Adam, and J. Talvacchio, March 1989, "Superconducting Stripline Resonator Performance," *IEEE Transactions on Magnetics*, Vol. 25, pp. 1104-1106.
32. Pond, J. M., P.F. Weaver, and I. Kaufman, Nov. 1990, "Propagation and Circuit Characteristics of Inductively Coupled Superconducting Microstrip," *IEEE Transactions on Microwave Theory and Techniques*, Vol. 38, No. 11, pp. 1635-1642.
33. McGinnis, D. P., and J.B. Beyer, Nov. 1988, "A Broad-Band Microwave Superconducting Thin-Film Transformer," *IEEE Transactions on Microwave Theory and Techniques*, Vol. 36, No.11, pp. 1521-1525.
34. Izadian, Jamal S., and Shahin M. Izadian, 1988, *Microwave Transition Design*, Artech House, Norwood, MA.
35. Hasnain, G., A. Dienes, and J.R. Whinnery, June 1986, "Dispersion of Picosecond Pulses in Coplanar Transmission Lines," *IEEE Transactions on Microwave Theory and Techniques*, Vol. MTT-34, No. 6, pp. 738-741.
36. Kajfez, D., and P. Guillon, 1990, *Dielectric Resonators*, Vector Fields, Oxford, MS.

## **GLOSSARY**

<b>CAD</b>	<b>computer-aided design</b>
<b>CPS</b>	<b>coplanar strip</b>
<b>CPW</b>	<b>coplanar waveguide</b>
<b>EM</b>	<b>electromagnetic</b>
<b>MMIC</b>	<b>Monolithic Microwave Integrated Circuits</b>
<b>MS</b>	<b>microstrip</b>
<b>SADC</b>	<b>superconducting analog to digital converters</b>
<b>SMA</b>	
<b>TEM</b>	<b>transverse electromagnetic</b>
<b><math>T_c</math></b>	<b>critical temperature</b>
<b>VSWR</b>	<b>voltage standing wave ratio</b>

## DISTRIBUTION LIST

### INTERNAL

#### A010

R. D. Haggarty

#### A030

R. W. Jacobus  
H. W. Sorenson

#### D011

B. A. Deresh

#### D050

R. A. McCown  
E. A. Palo  
E. N. Skoog

#### D053

R. T. Carlson

#### D058

J. R. Spurrier

#### D080

C. H. Gager  
J. M. Schoen

#### D090

A. Chu  
H. M. Cronson  
L. S. Metzger  
B. Rama Rao  
D. P. White

#### D091

W. C. Wilder  
C. A. Paludi

#### D092

M. E. Fitzgerald

#### D093

C. M. Plummer

#### D094

H. S. Babbitt, III  
P. D. Engels  
R. A. Haberkorn  
T. Lee  
S. Liberacki  
C. P. McClay (10 Unlabeled)  
M. L. Robinson  
E. F. Scherer  
S. Soares (10 Unlabeled)  
M. N. Solomon  
C. Tan  
P. S. Weitzman  
V. L. Wrick

#### D095

R. E. Eaves  
A. G. Montgomery

#### D096

W. J. Ciesluk  
L. R. D'Addario  
J. H. Lee  
G. F. Providakes

#### W010

J. M. Ruddy